



Deposited via The University of Sheffield.

White Rose Research Online URL for this paper:

<https://eprints.whiterose.ac.uk/id/eprint/230276/>

Version: Published Version

Article:

Marcial, J., Chesnutt, J., Neeway, J.J. et al. (2025) Alteration of archeological and natural analogs for radioactive waste glass under different environmental conditions. *npj Materials Degradation*, 9 (1). 102. ISSN: 2397-2106

<https://doi.org/10.1038/s41529-025-00624-4>

Reuse

This article is distributed under the terms of the Creative Commons Attribution-NonCommercial-NoDerivs (CC BY-NC-ND) licence. This licence only allows you to download this work and share it with others as long as you credit the authors, but you can't change the article in any way or use it commercially. More information and the full terms of the licence here: <https://creativecommons.org/licenses/>

Takedown

If you consider content in White Rose Research Online to be in breach of UK law, please notify us by emailing eprints@whiterose.ac.uk including the URL of the record and the reason for the withdrawal request.

<https://doi.org/10.1038/s41529-025-00624-4>

Alteration of archeological and natural analogs for radioactive waste glass under different environmental conditions

Check for updates

Jose Marcial¹ ✉, Julian Chesnutt¹, James J. Neeway¹, Eshchar Gichon², Clare L. Thorpe³, Zihua Zhu¹, Roman Golovchak⁴, Jozef Cebulski⁵, Przemyslaw Niedzielski⁶, Malgorzata Szostek⁷, Steven Luksic¹, Seungrag Choi¹, Ashley Kennedy¹, Rachel Anguish¹, Natalie C. Bohrmann¹, Adam Denny¹, Omri Yagel², John S. McCloy^{1,8}, Lesa R. Brown⁹, Russell J. Hand³, Jacqueline R. Hager¹, Andrew A. Plymale¹, Carolyn I. Pearce¹, Erez Ben-Yosef², Roland Hellmann¹⁰, Rolf Sjöblom¹¹, Michael J. Schweiger¹, David S. Kosson⁹ & Albert A. Kruger¹²

Approximately 200,000 m³ of legacy radioactive waste from plutonium production stored at U.S. Department of Energy's Hanford site will be immobilized in glass for disposal. The glass must limit radionuclide release into the environment for thousands of years, which is challenging to assess in laboratory experiments. Long-term alteration signatures on analog glasses can approximate how radioactive waste glass will perform over extended periods. Different glasses buried for tens to thousands of years at sites subject to variable climates and environments were selected for analysis. Surface altered layers that formed during glass corrosion were characterized. The thickness, chemistry, and morphology of surficial layers are discussed in terms of glass chemistry and burial conditions. Glass from arid environments, e.g., Timna (Israel), exhibited thinner surface layers (~2 μm) compared to glasses altered in humid conditions, e.g., Dobkowice (Poland: up to 59 μm), suggesting a role of burial environment and climate in long-term durability.

Glass waste forms are required to safely dispose of radioactive waste by immobilizing radionuclides and mitigating their release into the environment. At the Hanford site, a Department of Energy legacy nuclear waste site in Washington state, USA, hundreds of thousands of cubic meters of legacy radioactive waste from plutonium production will be immobilized in glass, with low activity waste (LAW) glass disposed in a near-surface integrated disposal facility (IDF). As described elsewhere¹, LAW glass will be prepared using a vitrifying supernatant and saltcake from the Hanford waste tanks. The glass must limit radionuclide release to the environment for thousands of years, which is challenging to assess in laboratory experiments. Central to radioactive waste management is a detailed understanding of the corrosion processes and a quantification of the corrosion rates of the glass waste form. However, laboratory glass

corrosion experiments have a limitation: their timeframes are considerably shorter than the timeframes over which radionuclides must be retained in a nuclear waste disposal site. Studies of natural analogs^{2–10} and anthropogenic glasses from archeological sites^{11–16} can help bridge this important gap. Using such glasses has significant theoretical and practical implications for nuclear waste management. By validating models used to assess waste form behavior with findings from natural and anthropogenic glasses, we can better understand the long-term performance of nuclear waste glasses. The alteration environments for these glass analogs vary in terms of temperature, pore fluid chemistry and pH, solid surface area to liquid volume ratio, percolation rate, and soil microbial communities. These variables must be considered when comparing analogs with proposed nuclear waste glasses¹⁰.

¹Pacific Northwest National Laboratory, Richland, WA, USA. ²The J. M. Alkow Department of Archaeology and ANE Cultures, Tel Aviv University, Tel Aviv, Israel. ³School of Chemical, Materials and Biological Engineering, The University of Sheffield, Sheffield, UK. ⁴Department of Physics, Engineering and Astronomy, Austin Peay State University, Clarksville, TN, USA. ⁵Institute of Physics, University of Rzeszow, Rzeszów, Poland. ⁶Faculty of Chemistry, Adam Mickiewicz University in Poznań, Poznań, Poland. ⁷College of Natural Sciences, Department of the Soil Sciences, Environmental Chemistry and Hydrology, University of Rzeszow, Rzeszów, Poland. ⁸School of Mechanical and Materials Engineering, Washington State University, Pullman, WA, USA. ⁹School of Engineering, Vanderbilt University, Nashville, TN, USA. ¹⁰Université Grenoble Alpes, CNRS, ISTERRE, Grenoble, Cedex 9, France. ¹¹Luleå University of Technology, Luleå, Sweden. ¹²US Department of Energy, Hanford Field Office, Richland, WA, USA. ✉e-mail: Jose.Marcial@pnnl.gov

Natural glass analogs, such as basaltic glasses (45–50 wt.% SiO₂), tektites (65–90% wt.% SiO₂), and obsidian glasses (70–75 wt.% SiO₂), are found in terrestrial environments. The thickness of the surface alteration layer (referred to as “palagonite”) can be used to semi-quantitatively evaluate the alteration rate of such natural glasses^{16,17}. Research suggests that the alteration mechanisms of natural, anthropogenic, and nuclear glasses are similar⁷. As an example, Techer et al.¹⁷ compared the alteration of basaltic glass (ages ranging from several thousand to a few million years) in natural environments with the alteration of basaltic glass and a reference nuclear waste glass (SON68) under laboratory conditions for periods of 4 days up to several hundred days. These authors pointed out some uncertainties and assumptions for natural samples, for example, the uncertainty in the nature of the altering environment and glass-solution contact time, and the assumption that the palagonite thickness can be directly compared to alteration layer thicknesses measured on glasses corroded in laboratory experiments. However, the results suggest that the mean alteration rate estimated from measured palagonite thicknesses was comparable to rates measured in closed system laboratory experiments for high reaction progress¹⁷.

Archeological glasses have also been used as analogs for comparison with alteration behavior predicted by nuclear waste glass models¹⁸. While archeological analogs are not compositionally identical to natural and nuclear glasses, they do contain most of the same major elements (alkalis, Si, Al, Fe, etc.)¹⁹. Archeological glasses also meet the criteria for an analog because information about the altering environment over the glass’s exposure time is often well documented. For example, two Roman glasses have been used as analogs to study long-term glass alteration behavior: (1) glass from a shipwreck off the coast of Embiez Island, France^{13–15}; (2) glass from the shipwreck *Iulia Felix* off the coast near Grado, Italy^{12,20,21}. These two glasses with similar compositions were altered in marine environments for nearly 1800 years. The *Embiez* glass was altered in open water in the Mediterranean Sea (15 °C). The *Iulia Felix* glass was altered in the Adriatic Sea (15 °C), which has a slightly different chemistry than the Mediterranean, and was covered with sand during its alteration. The *Embiez* glass shows significant cracking due to fast cooling during its fabrication, and an alteration behavior that is dependent on the size and the locations of the

cracks¹³. The same cracking phenomenon is observed in nuclear waste glass fabrication. The glass from the *Iulia Felix* shipwreck contains both colored²⁰ and colorless fractions²¹. The two glass fractions have compositions that vary only slightly; however, alteration of the colorless fraction results in an opaque white crust, mainly composed of silica (SiO₂), while the colored fraction shows alteration layers consisting of repeating lamellae²². Lamellae have also been observed in static tests of nuclear waste glass at acidic (pH = 4.1) conditions²³. This type of alteration has not been observed in laboratory testing at pH values near those expected in a disposal facility (pH 6–9), but the pH-dependence of lamellae formation needs to be confirmed²⁴. Wang et al.²⁵ have proposed that lamellae formation can be explained from a positive feedback between dissolution-induced cation release and cation-enhanced dissolution kinetics.

Waste glasses are typically subjected to short-term, accelerated laboratory tests to demonstrate that they are chemically durable for long periods. The kinetic behavior of these accelerated laboratory tests is then extrapolated over long time periods, but may not yield accurate predictions of glass durability over thousands of years. In addition, glass analogs have been used to predict the alteration of nuclear waste glasses during disposal in subsurface geological repositories^{6,9,10,19}. In particular, natural and archeological glasses can be used to assess how the alteration layers on the glass may have formed in response to near-field environmental conditions.

In this study, we characterize natural and archeological glasses from five near-surface sites exposed to different environmental and climatic conditions (e.g., average temperatures, extent of hydraulic saturation, etc.). A detailed description of the sites is provided, along with characterization data for the excavated samples. The range of environmental conditions these sites cover is relevant to the disposal of radioactive LAW glass at the near-surface, hydraulically unsaturated IDF Hanford site.

Unlike highly radioactive material, which will be buried deep underground in stable rock formations in a geological disposal facility, low activity radioactive waste does not require shielding and is suitable for disposal in shallower facilities closer to the surface. The Integrated Disposal Facility (IDF) is intended to be a near-surface disposal facility for radioactive LAW glass at the Hanford Site (Figs. 1 and 2A). It is a large, lined disposal trench excavated ~13 m deep into the Hanford sands in the Central Plateau at the

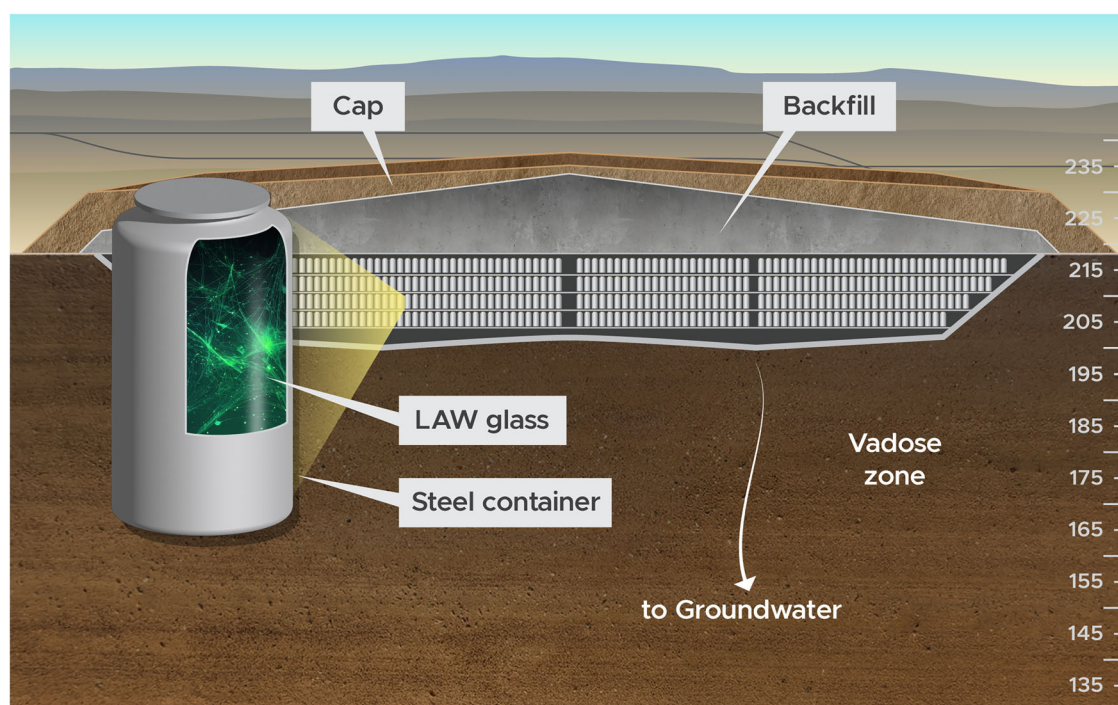


Fig. 1 | A schematic of the Integrated Disposal Facility (IDF) in the Central Plateau at the Hanford site. The view is a cross-section of the facility, and the dimensions are for information only.

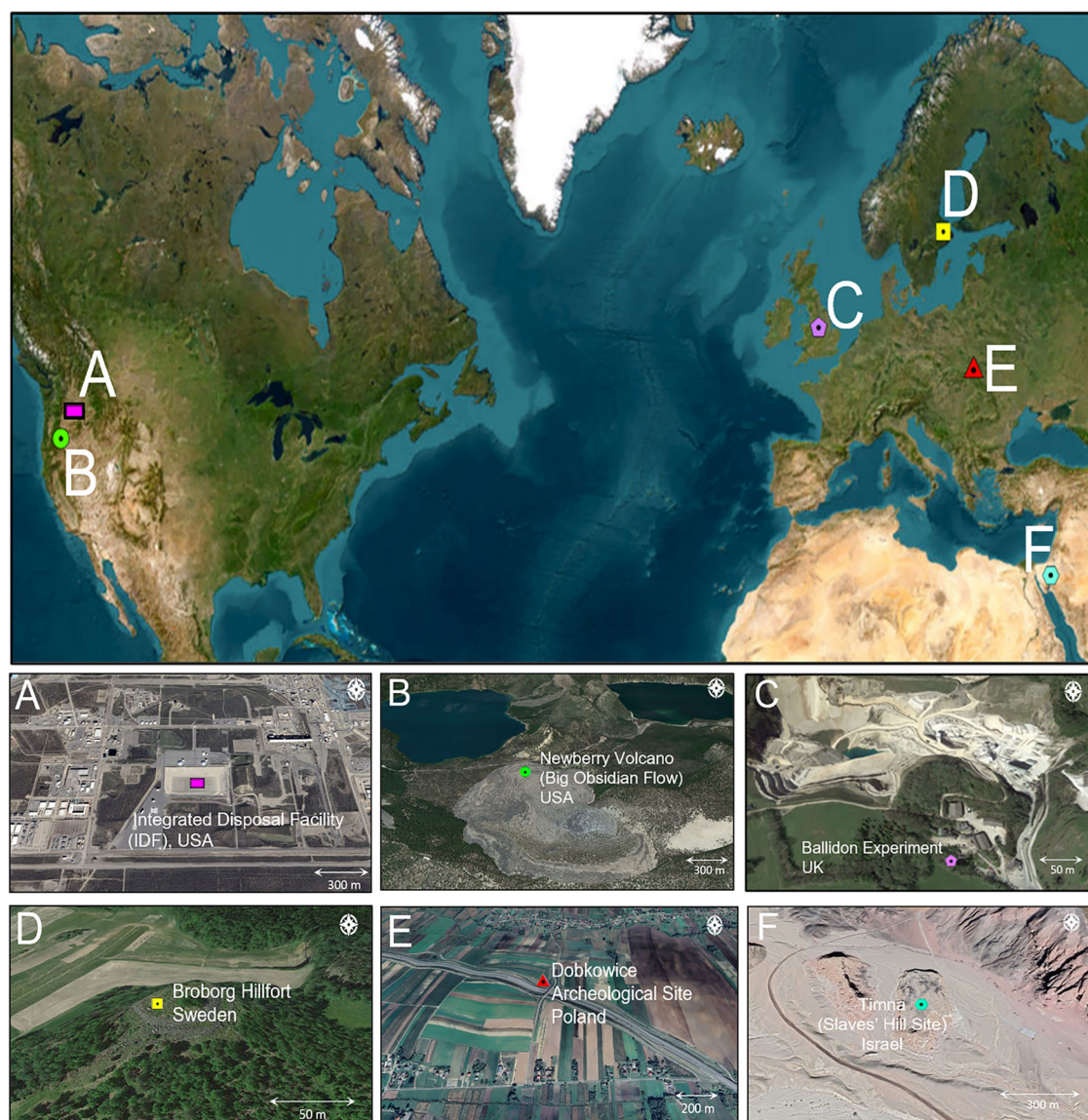


Fig. 2 | Location of natural and archeological analogs sites. A Hanford IDF, near Richland, WA, USA, B Newberry Volcano (Big Obsidian Flow), near Bend, OR, USA, C Ballidon Experiment Site, Tarmac Quarry, Derbyshire, UK, D Broborg Hillfort, Uppland, Sweden, E Dobkowiec Archeological Site, Subcarpathian Voivodeship, Poland, F Timna Site (Slaves' Hill), Timna Valley, Israel. The overview image was created using ESRI ArcMap; all others were created using Google Earth.

Hanford Site. The key engineered design features of the IDF consist of: (1) containers around the waste and a surface barrier placed above the waste containers to limit contact with water; (2) engineered backfill placed between and above waste containers to provide structural support after closure; (3) borosilicate glass waste forms that limit the release of contaminants due to the slow dissolution of the glass matrix. The key natural features consist of: (1) a semi-arid climate and shrub-steppe ecology that results in minimal natural recharge to the groundwater due to low annual precipitation rates and high evapotranspiration; (2) a thick vadose zone that delays the time it takes contaminants released from the source term to arrive at the saturated zone. At the Hanford Site, basalt is underlain by Tertiary continental sedimentary rocks and overlain by late Tertiary and Quaternary fluvial and glacio-fluvial deposits. The climate at the Hanford Site is mid-latitude semiarid desert. Daytime high temperatures in June, July, and August range from 17.2 °C to 27.9 °C but can exceed 40 °C. During the winter, temperatures generally range from -0.2 °C to 6.9 °C but can occasionally drop below -18 °C. The typical annual relative humidity is 54%, and the average annual

precipitation is ~180 mm, with about 38% as snow^{26,27}. At Hanford, winters are projected to be wetter and summers drier, with temperatures estimated to rise 1.7–5.6 °C this century, continuing the 0.83–2.2 °C rise from last century^{27,28}. The precipitation is expected to range from -10% to +20% from current levels to ~2080²⁹. The Hanford Site experienced massive glacial flooding ~13,000 years ago as the last Ice Age was ending. Temperatures rose 2.8 °C, and the climate became substantially (up to 50%) drier than today^{27,30}. The Hanford site has undergone considerable change in the last 100,000 years; annual precipitation ranged from 50–128% of present-day levels, with a -2.5 °C to 2.8 °C range in annual temperature^{27,30}. The future climate of the Hanford site is expected to be as variable as it has been in the past^{26,27}.

To establish limits on radionuclides that will be disposed of in the near-surface IDF, an assessment of impacts to groundwater resources must be made so that the concentration of radionuclides does not exceed the current drinking water standard. The assessment established a 1000-year compliance evaluation with additional analysis performed out to 10,000 years to determine peak elemental release³¹. To make this assessment, the alteration

behavior of the LAW glass in the near-surface environment of the IDF must be known.

Samples were chosen from specific analog sites to evaluate the following parameters: (1) how variation in surficial geology affects glass degradation; (2) effects of the environment on glass degradation; (3) comparison of sites with respect to the geology and current environment conditions, and possible environmental changes at the IDF; and (4) effect of hydraulic saturation (especially compared to the nominal conditions at the IDF). Several of these analog glasses are from archeologically significant sites, therefore, it was not possible to randomize sample collection. This resulted in an unintentional bias towards sample types that were more widely available for characterization. The site characteristics, as detailed below, vary in terms of (1) the amount of time the glass was buried, (2) the chemical composition of the glass, (3) the surficial geology, (4) the environment (precipitation and climate), (5) burial depth, and (6) site elevation. Table 1 summarizes the analog glasses chosen for study, Fig. 2 provides a map of the excavation sites, and Fig. 3 provides a timeline comparing relevant timescales (the alteration timescales for the analog sites will be described in the subsequent sections). Information on the geologic setting for each site is available in the supplementary materials.

The Broborg site (59°45'20" N, 17°57'06" E, elevation 49 m) Viking hillfort (Fig. 2E) was established ~ 375–550 CE¹⁹ in what is now the southeastern Uppland Province, ~25 km southeast of Uppsala. The technology and materials used to construct this hillfort are summarized by Sjöblom et al.³². Vitrified rock samples were collected from the Broborg site during multiple excavations (1982–1983, 1990 and 2017) and are described elsewhere^{33,34}. Bulk sample analyses of the granite and amphibolite rocks were presented by Ogenhall³⁵. Vitrified materials from the Broborg site were produced when the local amphibolite and granite were melted in situ^{32,36–38}. The vitrification of the amphibole-rich rock produced a dark Fe- and Mg-rich glass, while the vitrification of the granite yielded a clear Na- and Si-rich glass. The altered layers observed on excavated samples were compared to altered layers observed on excavated material that had been remelted to form coupons, which, in turn, were subjected to laboratory testing (vapor hydration test, VHT, product consistency test, PCT, and EPA method 1313)¹⁶.

Broborg's selection as an analog site provided an opportunity to study ancient glass buried in a soil that is a mixture of ancient mountain soil and more recent till-derived sandy clay loam³⁹. The overall climate of this site can be characterized as relatively humid and continental. Before the hillfort was constructed, temperatures were slightly warmer than the long-term average in the Roman Warm Period⁴⁰ (Fig. 3). When the fort was active, the Dark Age Cold Period (ca. 300–800 CE) was marked by temperatures below the long-term average⁴⁰. Volcanism in Iceland caused temperatures to plummet from 536 to 539 CE^{41,42}. The Medieval Warm Period saw an increase of 0.3 °C to 1.1 °C compared to the local maximum. After the maximum, another cooling trend occurred during the Little Ice Age (LIA) before reversing around 1600 CE with warming to 2000 CE^{40,43}.

The Timna site (Fig. 2F), situated in the Aravah valley of the southern Negev desert (Israel), is known for its well-preserved historic copper mining districts that reveal at least 7000 years of archeological evidence of metallurgical activity. The region's tectonic and hydrothermal activities, combined with the local lithologies, contributed to the formation of copper deposits⁴⁴. Ancient smelting sites provide evidence for copper production from the Copper Age to the Early Islamic Period. The vitrified slag samples from Timna described in the present paper were retrieved from copper smelting sites from the Early Bronze Age to the Early Islamic Age⁴⁵. Timna's primarily hot desert climate and arid soils contrast starkly with those of the other analog sites. The dominant soils in Timna are aridisols^{46,47}. These are dry soils with limited organic matter and weak soil structure. Due to low rainfall and high evaporation rates, they are often saline^{46,48,49}. Due to the limestone and chalk bedrock in regions around Timna, some soils exhibit a high calcium carbonate content, which can form hardpans or caliche layers⁵⁰.

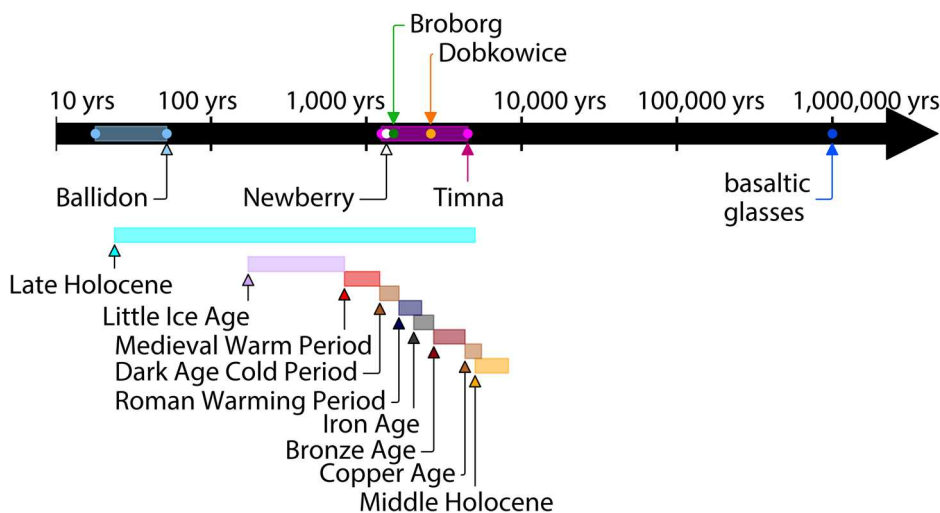
Hyper-arid conditions have dominated the Aravah Valley since the late Pliocene and early Pleistocene^{51–53} due to it being located in the rain shadow

Table 1 | Summary of glasses and alteration environments

Site	Type of glass	Origin and age (years)	Annual precipitation (mm)	Average air temperature (°C)	Elevation
Hanford, USA	Borosilicate	Wasteform for the disposal of low activity radioactive waste, not yet produced	~180	~12	IDF is 13 m deep, Hanford Site is 123 m above sea level
Timna, Israel	Melted Lower Cretaceous sandstones (with iron and copper oxides)	Copper slag, 1200–6000	30–15	~21	~300–450 m above sea level
Broborg, Sweden	Dark glass from melted amphibolite, clear glass from melted granite	Rocks melted in box-like structures around a hillfort, 1500	700–750	~4.6	50 m above sea level/near watershed
Ballidon, UK	Simulant Roman, Medieval, borosilicate, plate glass, soda lime, E-glass and lead optical	Experiment to understand glass corrosion under alkaline conditions, 50	908	9.2	Buried in a model burial mound comprised of limestone fragments, 282 m above sea level
Newberry, USA	Obsidian (ranging in composition from basalt, andesite, and rhyolite) and pumice	Last volcanic eruption: Big Obsidian Flow (BOF), ~ 1300–1400	~ 900	0	On top of the BOF, 2433 m above sea level
Dobkowice, Poland	Soda-lime-silica glass	Glass bead, 2600	700	0	Buried in grave ~1 m deep, 110 m above sea level

Fig. 3 | Timeline showing relevant time periods and ages of analogs, redrawn from Weaver et al.¹⁰².

For sites with analogs from multiple time periods, a colored rectangle describes the minimum and maximum ages. The timeline is shown in years before present, with present defined as 2024. For nuclear waste disposal, glasses are assessed for a 1000-year compliance evaluation with additional analysis performed out to 10,000 years to determine peak elemental release³¹.



of the Negev Highlands^{52–54}. The middle Holocene experienced significant climate fluctuations, ranging from hyper-arid periods to intervals with higher levels of precipitation⁵¹. This was superseded by drier conditions with fewer oscillations in rainfall in the late Holocene. In the Middle Bronze Age to the end of the Late Bronze Age, humidity increased, followed by a sudden and pronounced ~150-year dry event occurring from 1300 to 1200 BCE⁵¹. The late Iron Age was marked by increased aridity encompassing the Near East^{52,54}. Climate change has impacted Timna in the modern era. The twentieth and twenty-first centuries have seen a general trend of increasing temperatures, with precipitation patterns becoming more unpredictable and extreme⁵⁵.

The Newberry Volcano, near Bend in central Oregon and east of the Cascade Range on the western edge of the High Lava Plains, is one of the largest and most active volcanoes in the contiguous United States. Samples were collected in 2021 from Newberry's Big Obsidian Flow (BOF) (43°41'36" N, 121°13'45" W, elevation 2206 m) (Fig. 2B). Newberry last erupted ~1350 years ago (i.e., ~675 CE), resulting in the BOF^{56–59}. The obsidian from the most recent flow contains 72.8 wt.% SiO₂⁵⁶ and differs from most other rhyolitic rocks on the Newberry volcano in its much higher Rb/Sr ratio⁵⁷.

Newberry samples were chosen for this study due to their natural origin, unique chemical composition, and climate. The soils that contact the BOF are andisols. They are primarily derived from volcanic materials and tend to have a loamy texture with a balance of sand, silt, and clay, thereby allowing good water infiltration and root penetration⁶⁰. During the Medieval Climate Anomaly (MCA), the Newberry region experienced warmer and drier conditions⁶¹. During the LIA, cooler temperatures prevailed, with more frequent and extended wet periods influencing the region's ecosystems and human settlements⁶². Following the LIA, temperatures at Newberry and the overall Pacific Northwest region began to rise. The twentieth and twenty-first centuries have seen an acceleration of this warming trend, consistent with global climate change patterns. Recent studies have shown a decline in snowpack levels in the Oregon Cascades and a trend toward earlier spring snowmelt^{56,57,63}.

Dobkowice is a town in Jarosław county of Poland's Subcarpathian province, situated on the northern edge of the Carpathian Foredeep geological basin. Approximately 30 glass beads and other artifacts from the Bronze age were excavated from a crematory gravesite (49°55'48.92" N 22°42'55.85" E, elevation 218 m) (Fig. 2E)⁶⁴. The glass beads were made using a mixture of natron and lime/shells with sand⁶⁵. Because of their soda-lime-silica composition, these glasses are commonly referred to as natron glass or low magnesium glass (LMG). The beads, relics of the Jordanów culture, are estimated to be ~2600 years old (i.e., ~430 ± 150 BCE) and vary in color from light green to light brown⁶⁴. A local farmer discovered the site

in 1971 a few hundred meters northwest of the town. Excavations were conducted in the 1970s and 1980s, and finally in 2011–2012 before construction of a highway began^{66,67}. The Dobkowice site offers an opportunity to investigate anthropogenic glass buried in saturated soil in a relatively wet environment. The soil of the Dobkowice archeological site is an eutric fluvisol (soil base of saturation >50%)⁶⁸.

During the so-called Roman Warm Period (RWP) period (Fig. 3), Poland, along with the rest of Europe, likely experienced warmer climates⁶⁹, with relatively colder and drier winters offset by warmer and wetter summers⁷⁰. After the RWP, a cold period that lasted until about 800 CE brought cooler temperatures. During the last ~1000 years, until 1860 CE, summers and winters were colder than in previous millennia⁷⁰. The MCA, or Medieval Warm Period, was characterized by a warmer phase with temperatures that may have resembled modern pre-industrial times (Fig. 3)⁶¹. During the LIA, Poland and its surrounding areas experienced significantly colder winters and summers, which profoundly affected agriculture, settlements, and even warfare⁷¹. Post-LIA warming was observed in Dobkowice and the surrounding region. In the twentieth century, warming accelerated due to anthropogenic factors⁷². In recent decades, Poland has experienced higher temperatures, changes in precipitation, and increased extreme weather events such as heat waves and heavy rains, with an overall trend of rapid warming⁷³.

The Ballidon quarry site offers a controlled environment allowing the study of both natural and anthropogenic glasses. The Ballidon glass burial experiment (53°05'38"N, 1°42'08" W, elevation 228 m) (Fig. 2C) was initiated in 1963, based on preliminary results from buried glass samples from the Experimental Earthworks in Wareham⁷⁴. Various glasses were buried, including replicas of Roman soda-lime-silica glass, potash-lime-silica circa seventeenth century, and medieval glass^{75,76}. The pore water pH conditions at Wareham were acidic (pH 3.8–4.7), so the degradation of the glass samples was less representative of disposal conditions. Glass samples were more recently buried at Ballidon and experienced an alkaline (pH 7.8–8.2) limestone quarry environment^{74,76,77}. At Ballidon, samples were placed in a burial site originally measuring 3.5 m × 1.5 m and covered in limestone fragments, comprising pieces of crushed limestone (1 cm–8 cm fragments of calcite). At a sample depth of <20 cm, samples may occasionally have been affected by severe frosts. The soils at the Ballidon are loamy brown peaty top soils underlain by clay subsoils, with an average pore water pH of 9.6^{78,79}. Over the past 50 years, Derbyshire's climate has become slightly warmer and wetter, paralleling broader climatic trends across the UK^{74,76}. According to the UK Meteorological Office, the average temperature in the UK increased around 0.8 °C between 1961–1990 and 1991–2020^{80,81}. This increase was most substantial in central and eastern England, where some areas saw temperatures rise by more than 1.0 °C^{80,81}. Despite elevated

Table 2 | Comparison of select site sample compositions (wt%)

Component	MJS1	BB1b (Na/Si-enriched)	BB1b (Mg/Fe-enriched)	Dobkowice	Replica medieval glass (Hangleton)	Timna tuyère	Site 28 (representative of Timna samples A-G)	Site 201 (Timna sample H)	Site 34 (Timna samples I-K)	
Location	Newberry	Broborg		Dobkowice	Ballidon ⁹²	Timna				
SiO ₂	70.14	64.26	53.86	75.08	46.5	60.88	55.89	77.76	56.45	
Al ₂ O ₃	13.93	15.82	12.77	0.36	3.5	19.60	0.89	8.78	1.03	
Na ₂ O	4.76	3.70	2.78	17.76	0.7	0.57	0.44	0.47	0.55	
Fe ₂ O ₃	3.48	5.25	12.83	0.17	1.2	11.04	21.5	6.4	22.76	
CaO	0.88	3.33	8.73	7.29	21.6	2.21	5.07	1.19	1.53	
K ₂ O	4.04	4.81	1.39	0.11	16.4	1.63	0.92	1.14	1.25	
MgO	0.22	1.97	6.68	0.36	5.4	0.70	0.79	0.26	0.38	
MnO	0	0.10	0.43	0	0	0.02	1.71	0.01	4.73	
P ₂ O ₅	0	0.58	0.20	0.06	4.6	0.18	0.67	0.08	1.88	
TiO ₂	0.22	1.04	0.89	0	0	0.91	0.2	1.78	0.31	
ZrO ₂	0.08	0	0	0	0	0	0.06	0.04	0.11	
CuO	0	0	0	0	0	0.05	5.03	0.16	1.98	
BaO	0	0	0	0	0	0	0.09	0.01	0.33	
Cr ₂ O ₃	0	0	0	0	0	0	0.03	0.01	0.02	
Cl	0	0	0	1.01	0	0	0	0	0	
Others	0	0	0	0.32	0	0	6.71	1.91	6.69	
Total	97.74	100.87	100.38	102.53	99.9	97.786	100	100	100	
Method	EPMA						Chemical digestion, ICP-OES, ICP-MS			

precipitation conditions, there are intermittent drying periods during the summer months. These fluctuating environmental conditions, as compared to other disposal sites, may be responsible for their unique alteration signatures⁷⁶.

The experiment was initially planned to run for 512 years, with the extraction of samples from sites within the mound at increasingly-spaced time intervals: 1, 2, 4, 8, 16, 32, 64, 128, 256 and 512 years⁷⁴. The 64-year sample retrieval was brought forward in time due to interest in nuclear waste-form glasses. From 1986 onwards, simulant nuclear waste glasses, including glass formulations from the UK, USA, and Russia, have been buried in vacant sites at Ballidon for various periods of time.

Similar glass burial experiments have also been undertaken elsewhere, including Chalk River Nuclear Laboratories (CRNL) in Ontario, Canada (1959–1978)⁸², the Stripa granite mine, Sweden (1982)⁸³, the Boom clay in Mol, Belgium (1986)⁸³, the halite disposal facility at the waste isolation pilot plant (WIPP) at Carlsbad, New Mexico (1986)⁸⁴, and the Hanford lysimeter site (present day) in glacial lake deposits and gravel⁸⁵. To directly compare the effects of local environmental factors on glass alteration, the same simulant nuclear waste glasses have been buried at the Stripa, Mol, Ballidon, Carlsbad, and Hanford sites⁸³. A discussion of other near-surface burial sites is provided elsewhere⁸⁶.

Results

Analyses were performed on analog samples from the five sites, and results are discussed in terms of the chemistry of the analog glasses, followed by observations and measurements of the surficial alteration layers prepared in cross section (or in the case of the Dobkowice sample, one set of images was taken along the as-cut surface without mounting in resin or polishing). Table 2 provides measured bulk compositions for samples from the five sites. These bulk compositions were measured using either EPMA, or ICP-OES and ICP-MS following chemical digestion.

Timna

For the samples that were excavated from Timna, the twelve samples chosen for analysis were biased toward material with high glass contents. These 12 analogs include 11 glassy slag samples and one tuyère sample (the Timna-L

sample) that were taken from three smelting sites in or near the Timna Valley: site 28, site 34, and site 201. The tuyère sample (Site 34) is approximately 3150 years old⁸⁷. The tuyère was a ceramic nozzle forming part of the bellows that were placed inside the furnace, usually pointing down to direct a forced draught towards the lower charcoals. The tuyère withstood extreme heat inside the furnace, with the surrounding area reaching temperatures of approximately 1300–1500 °C, allowing for molten metallurgical slag to accumulate on the tuyère, which mostly vitrified on cooling⁸⁸. Site 28, named the Be'er Ora “Slag Valley,” was a big smelting camp located south of Timna Valley. Radiocarbon dating of samples from site 28 found that these materials mostly dated to the seventh to tenth centuries CE^{89–91}. Site 34, named “Slaves Hill,” has been a key site of the Central Timna Valley (CTV) project, which has been led by researchers from Tel Aviv University. It was excavated between 2012 and 2023 and has received the most attention of all Timna sites. Radiocarbon dating revealed that smelting occurred roughly between the late eleventh and tenth centuries BCE⁸⁷. Site 201 is located on top of a small hill on the western side of the Aravah, just 5 km north of Timna Valley. The CTV Project excavated Site 201 in 2020 to further understand technological developments associated with the very early history of extractive metallurgy. Radiocarbon dating suggests that the site was active at several periods, from the end of the late Copper (4000 BCE) to the Early Bronze Age.

Table 3 compares the amorphous contents of 12 Timna samples determined by XCT and XRD (using semi-quantitative Rietveld refinement) and lists the approximate ages of the samples. Figures 4 and 5 show XCT reconstructions and optical micrographs of 12 Timna samples, while Fig. 6 shows the corresponding XRD patterns. Overall, the more recent samples exhibit larger amorphous contents, which is attributed to improvement in the melting technology with time, leading to faster heating and cooling rates in the furnace.

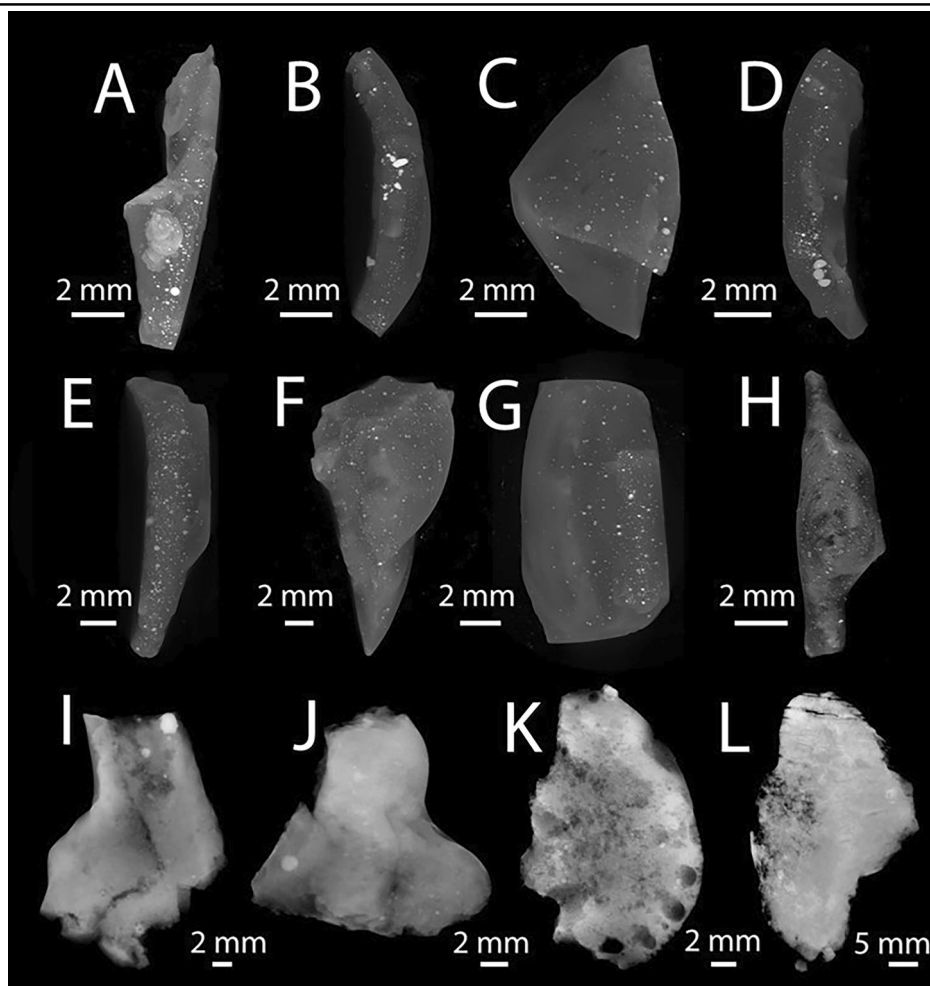
All the Timna samples show a thin surficial discoloration assumed to be an alteration signature. The surficial layer on the tuyère sample, which is a sample containing a large glass content, is not visible along the entire surface, but has a consistent thickness in the regions where it is observed. Figure 7 shows a ~2 μm thick surficial layer on a Timna sample obtained using SEM. The back-scattered electron (BSE) image shows heterogeneities in mass

Table 3 | Comparison of amorphous contents (measured by XCT and XRD) and sample ages for 12 Timna samples

Sample	XCT solid inclusions volume fraction	XCT amorphous volume fraction	XRD amorphous mass fraction	Sample age (years)	Sample location
Timna-A	3.1%	96.9%	91.1%	1200 ± 150	Site 28
Timna-B	0.1%	99.9%	92.8%	1200 ± 150	
Timna-C	0.1%	99.9%	97.7%	1200 ± 150	
Timna-D	0.1%	99.9%	99.3%	1200 ± 150	
Timna-E	0.1%	99.9%	90.8%	1200 ± 150	
Timna-F	0.1%	99.9%	89.8%	1200 ± 150	
Timna-G	0.1%	99.9%	97.8%	1200 ± 150	
Timna-H	14.40%	85.60%	21.7%	3100 ± 100	Site 34
Tuyère (Timna-L)	31.67%	68.33%	52.0%	3100 ± 100	Site 201
Timna-I	>90%	BQL	12.8%	4500 ± 200	
Timna-J	>90%	BQL	8.3%	4500 ± 200	
Timna-K	>90%	BQL	23.0%	4500 ± 200	

BQL below quantitative limit.

Fig. 4 | XCT reconstruction of Timna samples showing internal structure. Three-dimensional XCT reconstructions of 12 Timna samples (A–L). The greyscale values in the individual images represent the relative attenuation of X-rays, which is a function of mass density and show the distribution of inclusions and voids within the samples.

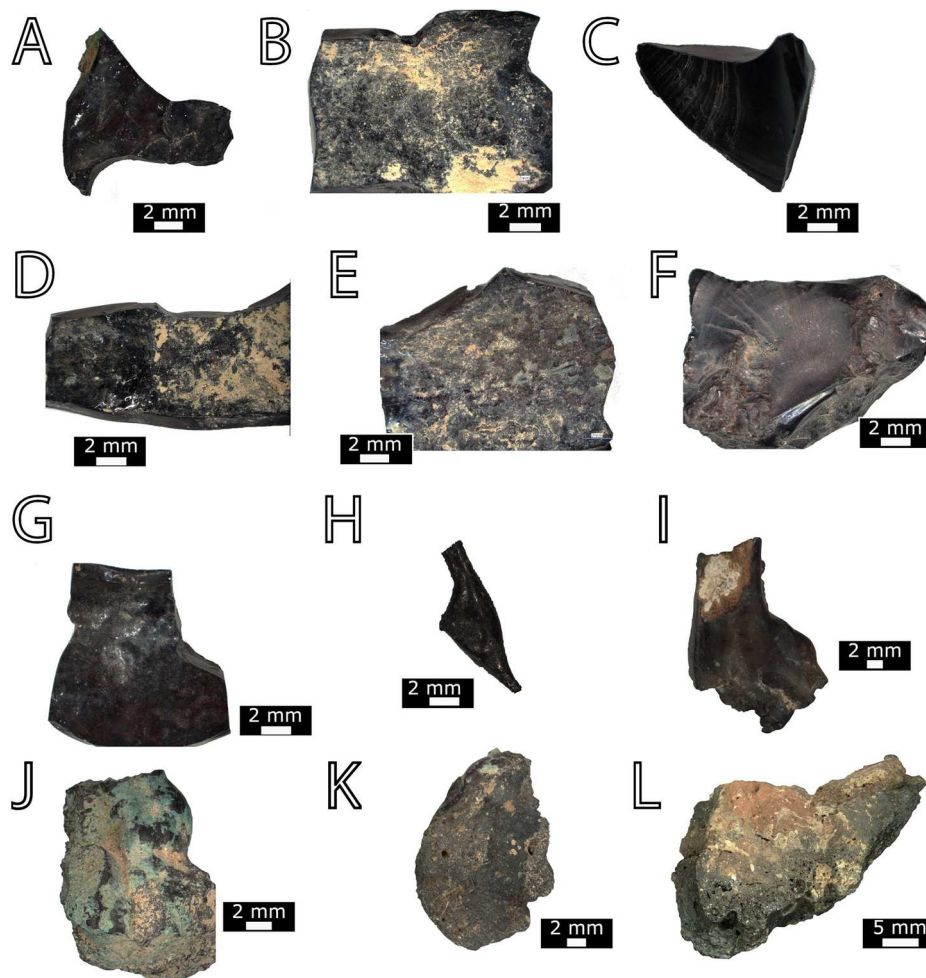


density within the layer, which are particularly noticeable when compared to the uniform, unaltered bulk material. Silicon shows no major change in concentration, whereas Mg is enriched in the layer. The interfacial gradient in the Mg concentration, at the scale of the image, is relatively sharp. The bulk material does show a few white circular regions, whose origin is not known. It is interesting that these circular areas are enriched in Cu and

depleted in Si. The BSE image also reveals the presence of a very thin dark band at the inner boundary between the surficial layer and the bulk, discussed in the next paragraph.

Figure 8 shows the same area measured by ToF-SIMS. The elemental maps show that the surficial layer has a constant thickness (~2–3 μm) and is enriched in H, Mg, Al, Si, K, and Cu (Cu just slightly), and depleted in Na

Fig. 5 | Optical microscopy images of 12 Timna samples showing physical appearance for comparison with XCT data on internal features. Optical microscopy images of 12 Timna samples (A–L).



and Ca. All enriched elemental maps (including Ca) display some heterogeneity, characterized by small, localized areas with higher-than-average concentrations. The surficial layer has an additional and extremely thin but non-continuous external layer that shows even higher enrichment in Mg, Al, Si, and K. This very thin layer is also evident in the SEM-BSE image of Fig. 8. Both the chemical maps and the BSE image show the same thin band at the inner boundary that separates the surficial layer from the bulk (Fig. 7). This black band may point to a physical gap, suggesting that the layer is not strongly bound to the bulk material.

Ballidon

Here, results are presented for a replica medieval glass sample (of potassium-lime-silica composition, designed to replicate a specific glass known as the “Hangleton linen smoother”⁹²) that was excavated from the Ballidon experimental mound⁷⁶. This sample was altered under near-surface conditions for a duration of 52 years before retrieval. The sample was mounted in epoxy, polished, and analyzed using EPMA. Figure 9 shows SEM-BSE images and elemental maps of the surface layer (SL) of the replica medieval glass sample. After 52 years, the alteration layer on this sample is considerably thicker than those on the Timna samples, ranging from 400 μm to 1000 μm . The SL is not homogeneous but appears to change abruptly in the sub-layer adjacent to the soil, with respect to the presence of gaps or pores between the much thinner layers. The elemental distributions of the various elements show an alternating pattern of bands corresponding to element depletion and enrichment. The SL, furthest from the pristine glass, appears more chemically separated (“banded”) whilst the younger alteration next to the pristine glass appears more uniform. The bands of enrichment and depletion also appear to be anti-correlated. The bands enriched in Al, Si, and

possibly K are spatially correlated with the same bands showing depletion in Ca, P, Fe, and Mg (panel C). The chemical boundaries of the bands are relatively sharp, except for Na and K, which are in part indistinct. The band widths vary in thickness (10–25 μm), which is particularly evident in the Fe, Si, P, and Ca maps. Such banding was also present in the Roman glass from the *Iulia Felix* shipwreck^{21,93,94}.

Dobkowitz

An SEM-BSE image of a polished section of a glass bead from the Dobkowitz burial site is shown in Fig. 10A. Surficial alteration of this sample takes the form of a distinct thin layer surrounding the entire sample. The layer appears to exhibit spalling, which is most likely an artifact created during sample embedding in epoxy. The actual boundary of the spalling is not strictly correlated to the boundary of the alteration layer with the bulk glass. The high-resolution SEM-BSE image in Fig. 10B shows that the layer is composed of a relatively homogenous ~ 50 μm -thick surficial layer (SL#1) having a sharp interface with the bulk glass. There is also a very thin and heterogenous over-layer (SL#2) that represents the topmost part of the alteration layer; note that these two layers resemble those in Fig. 8. The SEM-EDS map in Fig. 10C shows that the surficial layer can have variable thicknesses, here it is on the order of 50–100 μm . The principal alteration layer (SL#1) is depleted in Na, enriched in Si, and displays a more complex morphology, as evidenced, for example, by the Al-rich vesicle (this vesicle is further highlighted in Supplementary Fig. 1, which shows individual SEM-EDS maps of Fig. 10C). It is unclear if the Al-rich vesicle is the result of a glass alteration process or if it is soil that was incorporated into the surficial layer. This vesicle bears an uncanny resemblance to vesicles seen in oceanic basalt glasses that have been ascribed as being due to microbially-enhanced

dissolution⁹⁵. Supplementary Fig. 2 shows SEM-EDS maps overlaid on SEM-BSE images from a non-polished “as-is” fractured surface from the Dobkowice sample, confirming that SL#1 is Na-poor, Si-rich and is attached to the bulk glass, thereby confirming that the spalling in Fig. 10 is due to sample preparation.

The SEM-BSE and ToF-SIMS images in Fig. 11 reveal that in this portion of the Dobkowice sample, there exists a dominant alteration layer (SL#1) with a uniform thickness of approximately 50 μm. There is very little mass-density difference between SL#1 and the bulk glass. The large crack is

an epoxy-embedding artifact and should not be confused with the SL#1 interface with the bulk glass. The ToF-SIMS chemical maps in Fig. 11 illustrate that the principal layer (SL#1) is hydrated (as shown in the H map), enriched in Si, Ca, and just slightly in Mg, and depleted in Na and K. The principal alteration layer has a very thin external rim (SL#2) characterized by strong Al and K enrichment as previously observed by other researchers⁵⁴.

Broborg

Sample BB1b was originally excavated from the Broborg hillfort, as described in the literature^{16,36,96,97}. It was selected for study because it has a significant fraction of glassy material, and the surface appeared altered through natural processes^{96,98}. Figure 12 shows an optical microscopy image and SEM-EDS elemental maps of the sample prepared in cross-section (individual maps shown in Fig. S3). In Fig. 12, the term ‘bulk’ refers to a glassy phase that was created during the melting of the protolith rocks and ‘SL’ refers to the surficial layer. The surface of the bulk glass is predominantly mafic, as the mafic glass is two orders of magnitude less viscous than the felsic glass, and therefore very likely flowed over the felsic material⁹⁸. Compared to the bulk mafic glass, the surficial layer shown in Fig. 12B is enriched in Si and depleted in Na, Al, Mg, Ca, and Fe. The surficial layer in Fig. 12C is also depleted in Na and Fe, and enriched in Si. Ca is depleted, except for certain hotspots with elevated concentrations. The behavior of Mg and Al in the surficial layer is more complex, with areas of both enrichment and depletion. The textural and chemical heterogeneity of the bulk glass makes the evaluation of surficial layer formation challenging in samples from the Broborg hillfort.

SEM-EDS maps of a larger area of the Broborg BB1b sample are shown in Fig. 13, highlighting the surficial layers associated with the mafic region (individual maps shown in Fig. S4). The alteration layer is highly irregular in morphology and has an approximate average thickness of 13 μm. Some of this morphology may have a biological origin (e.g., see oval object on the left side of SL). The chemical composition of the altered layer differs from the amorphous matrix: Si is enriched, Al is depleted, and Fe, Mg, and Na are completely absent, having concentrations below the detection limit (see individual SEM-EDS elemental maps in Fig. S4). Figure 13 shows the textural and chemical heterogeneity of the bulk glass with feldspar needles, and irregularly shaped iron-bearing pyroxenes and spinels (identified by X-ray diffraction in Matthews et al.⁹⁶) that are present throughout the glassy matrix. These crystalline phases are also present at the interface to such an extent that the glass matrix is rarely in contact with the surficial layer. The aqueous alteration rates of crystalline silicates and spinels are predicted to be significantly slower than silicate glasses. It is uncertain whether alteration of the glass proceeded until the alteration front reached a crystallite, or if these phases crystallized near the surface of the original bulk glass. However, it can

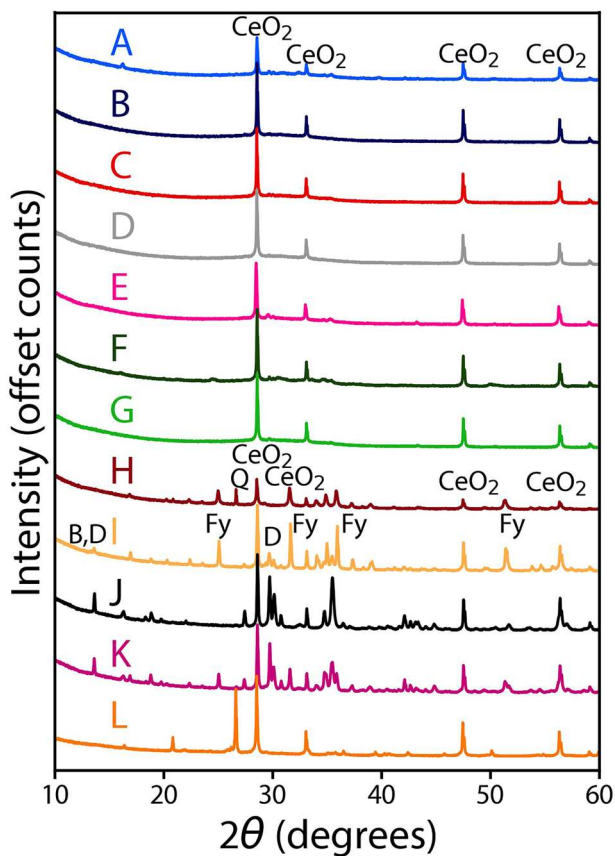


Fig. 6 | XRD patterns of Timna samples to assess phase distribution and amorphous Content. The XRD patterns of Timna samples (A–L) are shown after addition of a 5 wt.% CeO₂ internal standard. In the figure: Q-quartz (SiO₂), Fy-fayalite (Mg_xFe_{1-x}) SiO₄, D-diopside (MgCaSi₂O₆), and Bbirnessite (MnO₂·nH₂O).

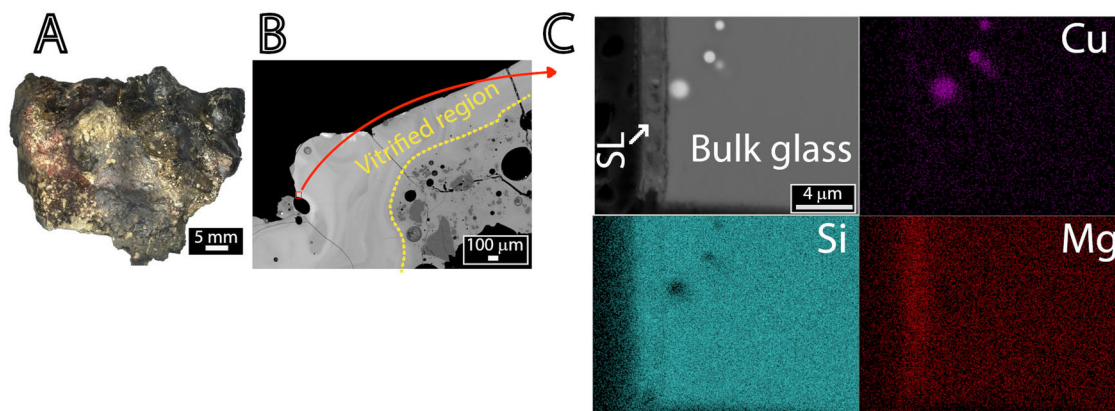


Fig. 7 | Optical and electron microscopy of Timna-L sample showing surficial layer. Comparison of: A Optical microscope image of partially vitrified Timna-L sample. B, C SEM-BSE (backscattered electron) images of partially

vitrified sample showing scale of surficial layer (denoted as “SL” in C). In B, a red arrow points from the approximate location of the elemental map shown in (C).

Fig. 8 | ToF-SIMS maps of partially vitrified Timna-L sample and the corresponding SEM-BSE image of the same area.

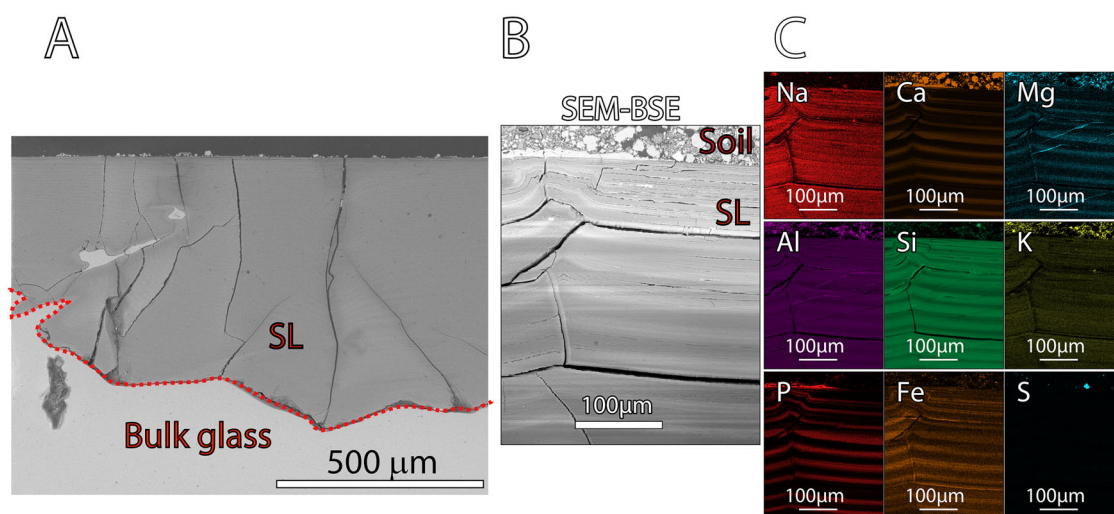
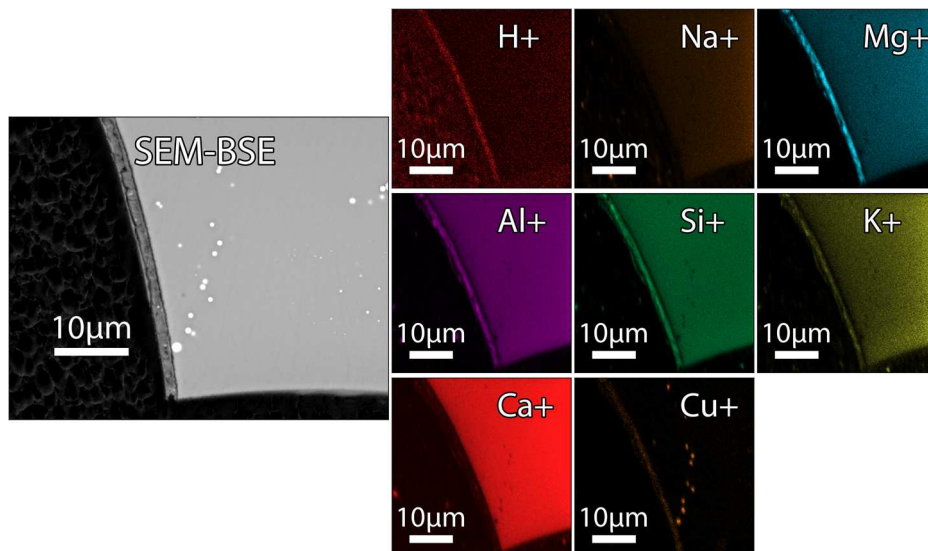


Fig. 9 | Analysis of surficial layer on replica medieval glass sample from Ballidon. **A** SEM-BSE image, **B** higher magnification SEM-BSE image and **C** EPMA-WDS maps of a replica medieval glass sample excavated from the Ballidon site showing a

surface layer (SL) with prominent depletion-enrichment banding. Approximate SL-bulk glass interface shown with a dashed line.

be hypothesized that the composition and structure of the underlying matrix had a direct impact on the surficial altered layer.

Newberry

Results are presented for three samples (MJS-1, BOF-6, and BOF-9) from the Newberry volcano Big Obsidian Flow. Samples BOF-6 and BOF-9 were both excavated in the same approximate vicinity; however, BOF-6 was partially covered in soil, while the BOF-9 sample was excavated from one of the walls of the obsidian flow. Sample MJS-1 was taken from the top of the flow. Figure 14 shows optical microscope and SEM-BSE images of the studied obsidian samples, including photographs taken from near the excavation sites of the three Newberry samples. Visually, the surfaces of MJS-1 and BOF-6 (Fig. 14A, E, respectively) both appeared white, while the surface of BOF-9 had a reddish tint (Fig. 14C). However, the BOF-6 surface was much more friable, while the surface of MJS-1 was consolidated. Both the MJS-1 and BOF-6 samples contained evidence of plant roots present on their surfaces.

The SEM-EDS elemental maps of sample MJS-1, in Fig. 14B, show a surficial layer that is relatively non-porous at this magnification and has a variable thickness, ranging from a few μm to $\sim 15 \mu\text{m}$, with an

average of $9 \mu\text{m}$. The SEM-EDS chemical map of the BOF-9 sample in Fig. 14D shows that the red-colored surficial layer is composed of a highly porous, sponge-like structure that is compositionally similar to the underlying obsidian glass, with a minor fraction of particles being either Fe or Na-rich. The SEM-EDS chemical map of the BOF-6 sample, shown in Fig. 14F, reveals a smooth surface that is amply covered with silicon-rich features that are most likely diatoms⁹⁹. At the scale of the analyses, there is no obvious evidence of an altered layer of significant thickness. Single element SEM-EDS maps of MJS-1, BOF-6, and BOF-9 can be found in Figs. S5–S7, respectively.

Figure 15 shows ToF-SIMS ion maps of the altered layer of sample MJS-1. The maps show a $\sim 10 \mu\text{m}$ -thick surficial layer with sharp chemical boundaries at both the inner and outer interfaces. The altered layer appears to be very heterogeneous with respect to its structure and composition, as shown in the SEM-BSE image (Fig. 15). This heterogeneity is also reflected in the chemical maps, which often show localized regions of enrichment and depletion. Na and K are generally depleted in this layer, while H, Mg, Al, Si, Ca, and Fe are enriched locally. The depleted and enriched layers are spatially coincident for all elements. The one exception is H, as this element displays two zones: (1) a prominent outer zone of elevated H enrichment

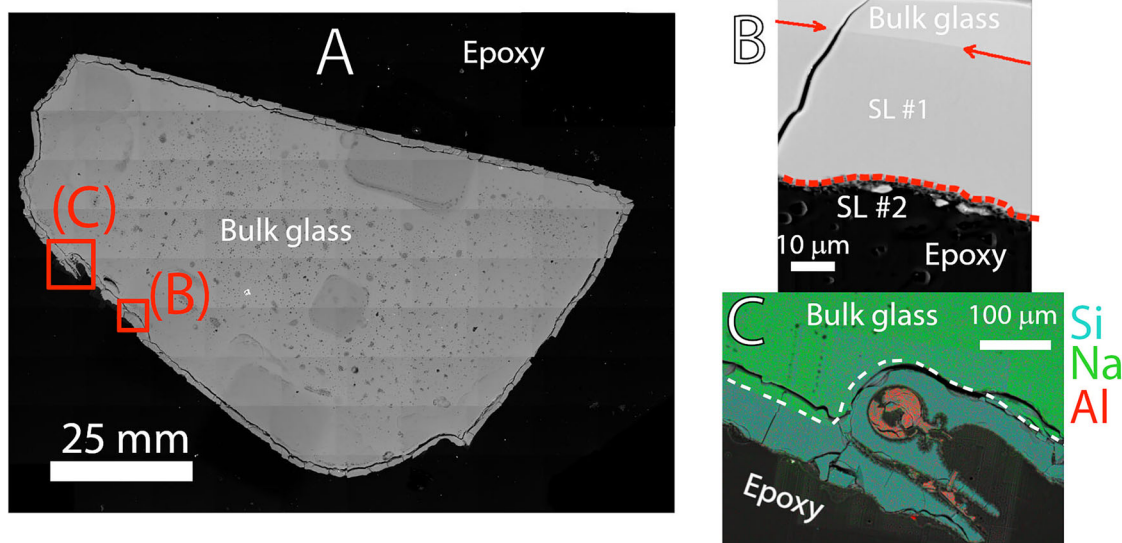
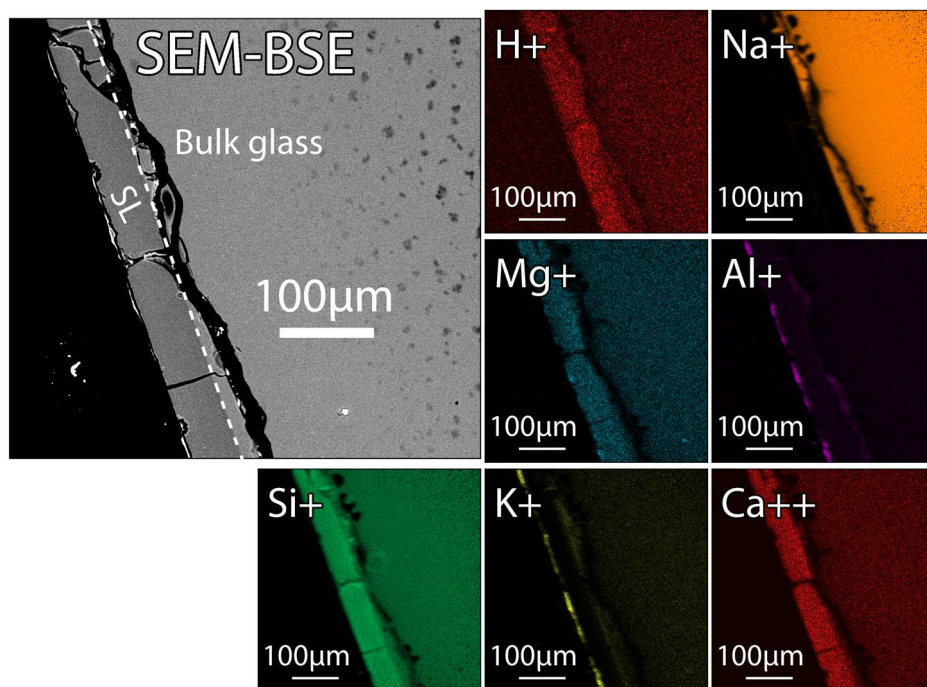


Fig. 10 | Analysis of bulk glass and surficial layer for a glass bead from the Dobkowice burial site. A SEM-BSE image of Dobkowice sample in cross-section. B SEM-BSE image showing two surficial layers (SL#1 and #2) that formed during

alteration. C SEM-EDS map overlaid on SEM-BSE image showing complex microstructure in one portion of the surficial layer SL#1. The small Al-rich growths are considered equivalent to SL#2.

Fig. 11 | SEM-BSE image and corresponding ToF-SIMS maps of the Dobkowice sample. The chemical maps show that the principal alteration layer (SL#1) is enriched in H, Si, Ca, and just slightly in Mg, whereas Na and K are depleted. Arrows demarcate the SL#1-bulk glass interface. The thin outer rim (SL#2) is enriched in Al and K. The prominent crack is an artefact.



~10 μm thick; and (2) an adjacent, inner zone ~4 μm thick that is characterized by H concentrations just barely above that of the bulk obsidian. Both H zones have relatively sharp boundaries at the scale of the image. This contrasts with the H map of the Timna sample (Fig. 8), which showed only one layer of H enrichment with sharp interfaces.

Discussion

The natural and archeological analogs presented here were exposed to different environments for different lengths of time. The analogs were of different chemistry, a parameter that is intimately tied to technological developments, including the ability to melt materials at increasingly higher temperatures due to improvements in the high-temperature processing

technologies that were employed, as well as the chemistry of the primary material sources used (important for controlling such factors as chemical impurities and oxidation state¹⁰⁰). The factors of environment, length of time, and chemical composition of the starting material had an influence on the chemistry and morphology of the surface layers and secondary phases that developed in contact with the unaltered bulk glasses. These factors are summarized along with average altered layer thicknesses in Table 4. The use of altered layer thicknesses to compare and estimate rates of glass corrosion should be viewed as very approximate for many reasons. One reason is molar volume changes between the unaltered glass and the phase(s) making up the altered layer. Moreover, the effects of porosity in the altered layer also must be considered. It also cannot be excluded that over time, during burial

Fig. 12 | Optical microscopy and SEM-EDS elemental maps of Broborg sample BB1b in cross-section. A Optical microscopy image of Broborg sample BB1b with red arrows showing the location mapped by SEM-EDS. B, C SEM-EDS elemental maps overlaid on SEM-BSE. SL surficial layer.

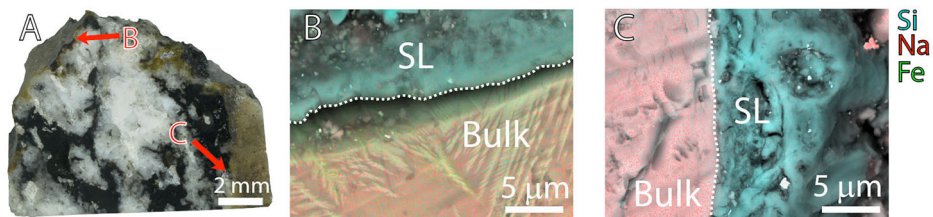


Fig. 13 | SEM-EDS maps of Broborg sample BB1b showing a surficial layer (SL) that formed in contact with the mafic glass. The arrows indicate the interface between bulk glass and the SL.

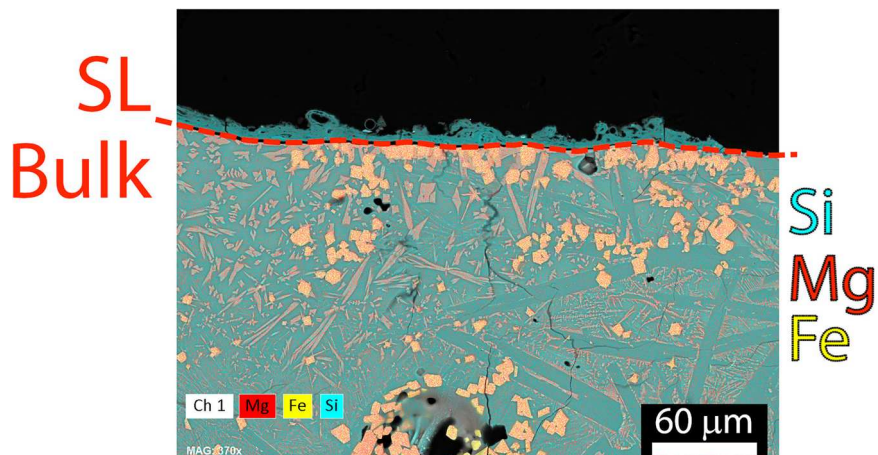
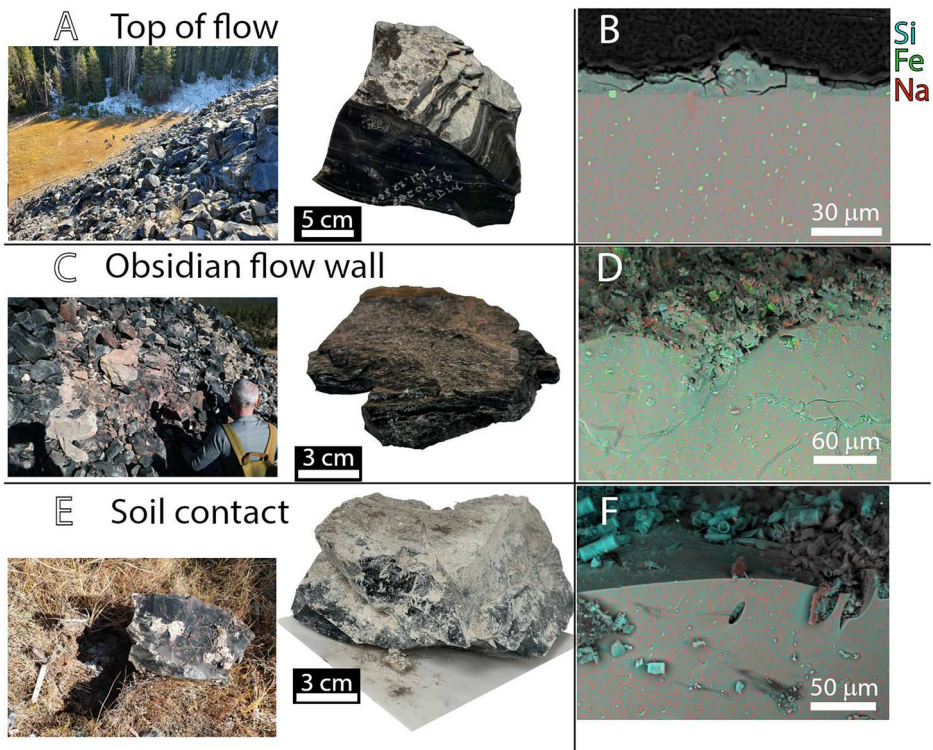


Fig. 14 | Optical microscopy and SEM-EDS elemental maps of obsidian samples from Newberry. A, C, E Photographs of Newberry obsidian outcrops and samples MJS-1, BOF-9, and BOF-6. B, D, F Corresponding cross-sectional SEM-EDS elemental maps of the surface regions and underlying matrix (individual EDS maps are provided in Figs. S5–S7).

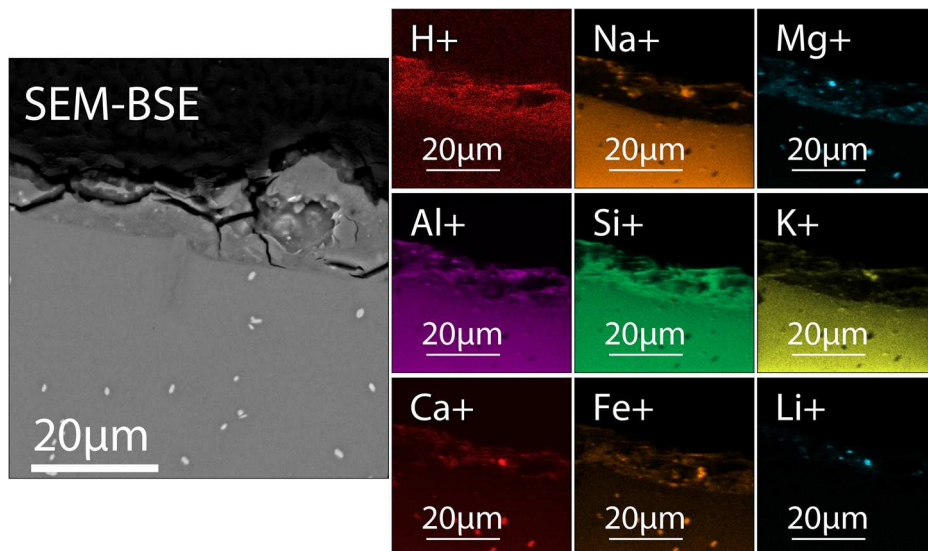


and then retrieval from the soil, some of the surface altered layers may have lost their structural integrity, causing secondary phases to peel or break off, thereby making the altered layers incomplete and thinner.

The archeological samples described in this study were excavated from near-surface conditions in hydraulically unsaturated environments. This is important as the information garnered from the studied samples can be

used to support the disposal of LAW glass at the Hanford site IDF. The nominal conditions at the Hanford IDF are an average subterranean temperature of 15 °C at 7.6-m depth, with an annual rainfall of ~180 mm¹⁰¹. After the waste and associated backfill have been placed in the facility, it will be covered with an engineered surface barrier. An infiltration rate of 0.5 mm/year is assumed while this barrier is intact, with the infiltration rate

Fig. 15 | SEM-BSE image and ToF-SIMS maps of Newberry obsidian sample, MJS-1.



increasing to 3.5 mm/year once the barrier has degraded (after ~500 years)¹⁰¹. Water infiltrating through the backfill will chemically react with the dominant minerals present, which are mostly comprised of silica, as well as some carbonates. The carbonates minerals will lead to buffering of the pore water to neutral-to-mildly alkaline pH conditions. The IDF temperatures and annual rainfall quantities are closer to those of Timna than the other analog sites. The glass compositions expected at the IDF are different from the glasses from the analog sites, having lower Si, Fe, and Al, higher Na, as well as components that are not present in the analogs, including B, Li, V, and Sn. The Ballidon site and other field-testing sites will provide important data on the alteration of compositionally relevant borosilicate glasses in near-surface conditions relevant to the Hanford IDF. Analysis of alteration observed on archeological and modern glasses (including one borosilicate composition) buried at the Ballidon site for 52 years is described in Thorpe et al.⁷⁶. Furthermore, analysis of US and UK nuclear waste type glasses buried for 18 and 20 years, respectively, is underway and includes borosilicate, silicate, and Fe-phosphate compositions. An additional test with buried LAW glass samples has also been underway since 2019, and data from those tests will be relevant to glass behavior in the IDF⁸⁶, even though the duration of those tests is much less than that achievable with the archeological glass samples.

The present work characterizes the surficial alteration features of natural and archeological glasses as a function of the burial environment and the bulk glass composition. The characterizations that were performed confirmed that the samples contained a significant fraction of glassy material. These glassy materials were subjected to alteration under near-surface conditions for periods exceeding 1000 years and fulfill the criteria to be considered as an alteration analog, since they^{4,6,102}: (1) are of a known or determinable *chemistry* (e.g., composition and structure); (2) are from a known or determinable *alteration environment* (e.g., exposure time, biological contact, solution chemistry, etc.); (3) are of a known or determinable *provenance* following its excavation (e.g., storage conditions, sampling history, conservation/restoration, etc.); and (4) are measurably *altered*. The physico-chemical characterizations revealed that differences in the chemical composition of the original samples significantly affected their chemical durability. The data in Table 4 suggest that the average annual air temperature and annual precipitation also have a measurable effect on the observed thickness of the altered surficial layer. Due to the nature of the analogs and their environments (lack of duplicates, different compositions, different temperatures, different rainfall, etc.), it is challenging to isolate the parameter that has the greatest effect on surficial layer thickness, and further characterization of samples from additional sites is needed in the future. However, the data show that samples altered in the arid Timna environment

have thinner surface layers than samples subjected to greater annual precipitation levels.

It is important to note that air temperature and average precipitation do not fully parameterize the exposure conditions for these samples, and that future work will investigate the influence of the soil pore water chemistry and the local microbial community on glass alteration. During efforts to characterize and assess the Broborg glasses as alteration analogs, evidence of microbial interaction with the glass surfaces was observed via SEM¹⁹. Further microscopic and spectroscopic analyses showed glass alteration (chemical and morphological) consistent with microbial activity, evidenced by surficial pitting beneath microbes, suggesting a microbial component to glass corrosion¹⁰³. Bacterial and fungal communities can colonize a variety of natural and synthetic materials, including rock and glass, by forming complex biofilms on the surfaces³³. These microbial biofilms are known to weather these material surfaces using biophysical and biochemical processes (such as penetrating within cracks, producing extracellular polysaccharides, and secreting organic acids)¹⁰⁴. Decades of research have established that microbial communities can persist and even thrive in harsh and toxic environments, suggesting the potential for biotic processes to influence the alteration of vitrified low-level nuclear waste after storage in near-surface geological facilities^{33,103,105,106}. However, most studies evaluating the long-term durability of vitrified nuclear waste glass have focused on the abiotic degradation of these materials in sterile environments¹⁰⁴. While the presence of microbes in these geological facilities is recognized^{107,108}, only a few studies have attempted to characterize and extrapolate the observed short-term microbial impacts to predict the long-term (i.e., thousands of years) bio-alteration of vitrified nuclear waste, and this is therefore an ongoing area of research^{33,104,109,110}.

To conclude, the knowledge obtained on how different environmental factors influence the alteration of vitrified archeological samples can be applied to vitrified nuclear waste materials. The subsequent incorporation of these factors into performance assessment models will allow for the development of a more holistic long-term prediction of the vitrified material durability under field conditions.

Methods

One of the main goals of the present study is to provide a general physical and chemical characterization of altered glass analogs recovered from the five sites. The techniques used provide information at various scales, with a maximum of micrometer-spatial resolution. Future work will involve techniques that have much higher spatial and mass resolution, such as transmission electron microscopy (TEM), atom probe tomography (APT), TEM-tomography, nano secondary ion mass spectrometry (nanoSIMS),

Table 4 | Summary of analog glass site data

Site and sample	Average SEM surficial layer thickness, μm	Average air temperature and annual precipitation	Sample age	Description of chemical and mineralogical makeup	Analog advantages	Analog limitations
Timna Tuvère	2 ± 0.2	15 °C, 25 mm annual rainfall. Arid with periodic floods ⁵²	3150 ± 50 years	Copper slag (iron-rich glass with fayalite and copper-rich inclusions)	Various alteration timescales, arid, amorphous, known provenance, near surface	Open system, heterogeneous, more arid than IDF, limited alteration
Broborg-BB1b	8 ± 2 (felsic glass), 13 ± 10 (mafic glass)	5 °C, 572 mm annual rainfall ⁹⁶	1500 years	Either mafic-derived glass + spinel + pyroxene or felsic-derived glass + quartz + feldspar	Different glass chemistries, known provenance, near surface	Heterogeneous, challenging surface analyses, more rain than IDF
Ballidon	Variable, depending on sample (>400 μm for replica medieval glass)	9–10 °C, 908 mm annual rainfall ⁹¹	18–52 years	Silicate, borosilicate, lead-silicate and Fe-phosphate compositions (US, UK and Russian nuclear waste glass)	Different glass chemistries, controlled experiments, high rainfall, near surface	Short alteration timescale, cooler and more rain than IDF
Newberry-MJS-1	9 ± 6	0 °C, 635 mm annual rainfall ^{116,117}	1350 years (most recent lava flow)	Obsidian	Homogeneous, natural, known provenance	Not buried, only one glass chemistry
Dobkowitz	59 ± 2	0 °C, 700 mm annual rainfall ¹¹⁸	2600 years	Soda-lime-silica glass	Various alteration timescales, arid, amorphous, known provenance, near surface	Open system, more rain than IDF, limited number of samples, simple composition

etc., to better characterize the altered samples. Such high-resolution analysis techniques have been shown to provide significant insights into the interfacial region that delimits the boundary between the non-altered parent material and overlying authigenic surface layers (SL). Atomic scale measurements are crucial for future interpretations of the mechanisms of alteration^{95,111–113}.

Optical microscopy, scanning electron microscopy (SEM), and electron probe microanalysis (EPMA)

Optical microscopy was performed with a Keyence VHX 7000 optical microscope. Samples were observed either ‘as received’, to evaluate surficial layers prior to any additional sample preparation involving exposure to water, or processing for polished sections for detailed characterization of the chemistry and morphology. Polished sections were made by first fracturing bulk material, embedding grains in epoxy, and then polishing sequentially with 240, 320, 400, 600, 800, and 1200 grit SiC abrasive paper in the presence of water (exposure to water during polishing is on the order of minutes compared to the hundreds of years the archeological samples have been in contact with water). The very limited exposure to water should have a negligible impact on alteration layer thickness and morphology). This was followed by polishing with a 1- μm diamond paste suspension.

Much higher spatial resolution imaging of polished sections was performed using a JEOL 7001 F SEM operated with a 15 kV accelerating voltage and 13 nA probe current. Energy-dispersive spectroscopy (EDS) analyses were performed with a Bruker Xflash 6 60 X-ray detector with a spectral resolution of 129 eV. Energy-dispersive X-ray spectra were processed using Bruker Esprit v2.1 software. Higher accuracy chemical composition measurements were made by electron probe microanalysis (EPMA) using a JEOL 8530 instrument operated with a 15 kV accelerating voltage and 20 nA probe current. Wavelength-dispersive spectroscopic (WDS) measurements were made with five spectrometers for high-energy resolution compositional measurements and analysis of light elements.

X-ray computed tomography

The internal 3-D microstructure of the samples was analyzed using X-ray micro-computed tomography (micro-CT) using a Thermo Fisher Scientific Heliscan Micro-CT system. Samples were mounted on styrofoam and scanned with an 80 kV *p* unfiltered microfocus X-ray source with a <1.5 μm diameter focal spot. Projections were acquired in a space-filling trajectory with a detector shift applied to help lessen the impact of pixel-specific artifacts. The acquired projections were reconstructed on a GPU cluster using iterative methods, yielding digital 3D volumes with voxel sizes around 5 μm^3 . Image segmentation was performed on the X-ray projections to partition the projections into: (1) bulk phase of the samples (assumed to be the amorphous phase); (2) bright inclusions (assumed to be crystals); (3) voids; and (4) background. The segmented projects were then stitched together to form a reconstructed 3-dimensional representation of the samples. The voxels corresponding to the amorphous phase were summed and normalized to the total volume of the amorphous and crystalline phases.

X-ray diffraction (XRD)

XRD was performed with a Bruker Advance D8 X-ray diffractometer using a Cu K α X-ray source operated at 40 kV and 40 mA. Samples were either in bulk form or fine powders produced using a tungsten carbide mill. For semi-quantitative amorphous fraction analysis, sample powders were mixed with a 5 wt.% CeO₂ internal standard. XRD scans were collected from 5–70° 2 θ with a step size of 0.015° and a dwell time of 30 s. Phase identification of XRD patterns was carried out with EVA 4.0 using the PDF4+ database from the Inorganic Crystal Structure Database (ICSD). Rietveld refinement was used for semi-quantitative analyses of the amorphous sample fractions with TOPAS 4.0 software.

Time of flight secondary ion mass spectroscopy (ToF-SIMS)

ToF-SIMS measurements were performed using a ToF.SIMS5 instrument (IONTOF GmbH, Münster, Germany). ToF-SIMS has many advantages

over SEM-EDS, including improved elemental detection limits and the ability to measure hydrogen (H). The distribution of H in the alteration layer of polished analog samples was measured using experimental conditions optimized for high signal-to-noise (S/N) ratios of H¹¹⁴. A 25.0 keV Bi⁺ beam was used as the analysis beam to collect positive secondary ion maps of the following ions: H⁺, Li⁺, Na⁺, Ca⁺⁺, Ca⁺, ³⁰Si⁺, Si⁺, Al⁺, Mg⁺, C⁺, K⁺, Cu⁺, and ⁵⁴Fe⁺. A 1.0 keV O₂⁺ sputter beam with 240 nA current was used before and during analysis to remove surface contamination and control the hydrogen background. The O₂⁺ beam was scanned over a 700 × 700 μm² area for 600 s before data collection to remove surface contamination. During the collection of ion maps, the instrument was operated in a non-interlaced mode. The Bi⁺ beam was focused to a 400 nm diameter with a beam current of 1.70 pA at 20 kHz frequency. Maps were acquired over 200 × 200 μm², 150 × 150 μm², or 50 × 50 μm² areas with 256 × 256 pixels. During non-interlaced mode imaging collection, each cycle was composed of three steps: (1) the O₂⁺ beam was scanned over the sample for 1 s to remove H adsorbed on the surface to control the H background, (2) a 0.5 s pulse was used for charging control so that reasonable signal intensity could be achieved, (3) 2 scans for ion map collection, with 256 × 256 pixels per scan. A total of 50–200 scan cycles were accumulated during data collection.

Chemical digestion and aqueous elemental analyses

Chemical digestion was carried out by microwave-assisted acid digestion. Inductively coupled plasma-optical emission spectroscopy (ICP-OES) analysis was performed on an Agilent 5110 VDV (Agilent Technologies, Santa Clara, CA) for major elements. Inductively coupled plasma-mass spectrometry (ICP-MS) was performed with a Perkin Elmer model NexION 2000B for trace elements (i.e., Cr and Zr). The chemical digestion procedure and subsequent elemental analyses were performed following test protocol USEPA3052B¹⁵.

Data availability

Data sets generated during the current study are available from the corresponding author on reasonable request.

Received: 1 January 2025; Accepted: 3 June 2025;

Published online: 05 August 2025

References

1. Marcial, J., Riley, B. J., Kruger, A. A., Lonergan, C. E. & Vienna, J. D. Hanford low-activity waste vitrification: a review. *J. Hazard Mater.* **461**, 132437 (2024).
2. Crovisier, J.-L., Advocat, T. & Dussossoy, J.-L. Nature and role of natural alteration gels formed on the surface of ancient volcanic glasses (Natural analogs of waste containment glasses). *J. Nucl. Mater.* **321**, 91–109 (2003).
3. Techer, I., Lancelot, J., Clauer, N., Liotard, J. M. & Advocat, T. Alteration of a basaltic glass in an argillaceous medium: the Salagou dike of the Lodève Permian Basin (France). Analogy with an underground nuclear waste repository. *Geochim. Cosmochim. Acta* **65**, 1071–1086 (2001).
4. Miller, W., Chapman, N., Alexander, R., McKinley, I. & Smellie, J. and Department of the Environment, London (United Kingdom). Her Majesty's Inspectorate of Pollution. "Natural Analogue Studies in the Geological Disposal of Radioactive Wastes". (1994).
5. Lutze, W., Malow, G., Ewing, R. C., Jercinovic, M. J. & Keil, K. Alteration of basalt glasses: implications for modelling the long-term stability of nuclear waste glasses. *Nature* **314**, 252–255 (1985).
6. Ewing, R. C. Natural glasses: analogues for radioactive waste forms. *Mater. Res. Soc. Symp. Proc.* **1**, 57–68 (1979).
7. Techer, I., Advocat, T., Lancelot, J. & Liotard, J. M. Basaltic glass: alteration mechanisms and analogy with nuclear waste glasses. *J. Nucl. Mater.* **282**, 40–46 (2000).
8. Malow, G. & Lutze, W. Alteration effects and leach rates of basaltic glasses: implications for the long-term stability of nuclear waste form borosilicate glasses. *J. Non-Cryst. Solids* **67**, 305–321 (1984).
9. Libourel, G. The use of natural and archeological analogues for understanding the long-term behavior of nuclear glasses. *Comptes Rendus Geosci* **343**, 237–245 (2011).
10. Ewing, R. C. & Roed, G. Natural analogues: their application to the prediction of the long-term behavior of nuclear waste glasses. *Mater. Res. Soc. Symp. Proc.* **84**, 67–83 (1987).
11. Michelin, A. et al. Effect of iron metal and siderite on the durability of simulated archeological glassy material. *Corros. Sci.* **76**, 403–414 (2013).
12. Ryan, J. et al. "Ancient Roman Glass Characterization for use in Corrosion Modeling." PNNL-21847. *Pacific Northwest National Laboratory, Richland, WA* (2012).
13. Verney-Carron, A., Gin, S. & Libourel, G. A fractured roman glass block altered for 1800 years in seawater: analogy with nuclear waste glass in a deep geological repository. *Geochim. Cosmochim. Acta* **72**, 5372–5385 (2008).
14. Verney-Carron, A., Gin, S., Frugier, P. & Libourel, G. Long-term modeling of alteration-transport coupling: application to a fractured Roman glass. *Geochim. Cosmochim. Acta* **74**, 2291–2315 (2010).
15. Verney-Carron, A., Gin, S. & Libourel, G. Archeological analogs and the future of nuclear waste glass. *J. Nucl. Mater.* **406**, 365–370 (2010).
16. Nava-Farias, L. et al. Applying laboratory methods for durability assessment of vitrified material to archaeological samples. *npj Mater. Degrad.* **5**, 57 (2021).
17. Techer, I., Advocat, T., Lancelot, J. & Liotard, J. M. Dissolution kinetics of basaltic glasses: control by solution chemistry and protective effect of the alteration film. *Chem. Geol.* **176**, 235–263 (2001).
18. Zanini, R., Franceschin, G., Cattaruzza, E. & Traviglia, A. A review of glass corrosion: the unique contribution of studying ancient glass to validate glass alteration models. *npj Mater. Degrad.* **7**, 38 (2023).
19. Weaver, J. L. et al. Pre-viking Swedish hillfort glass: a prospective long-term alteration analogue for vitrified nuclear waste. *Int. J. Appl. Glass Sci.* **9**, 540–554 (2018).
20. Silvestri, A. The coloured glass of Iulia Felix. *J. Archaeol. Sci.* **35**, 1489–1501 (2008).
21. Silvestri, A., Molin, G. & Salviulo, G. The colourless glass of Iulia Felix. *J. Archaeol. Sci.* **35**, 331–341 (2008).
22. Silvestri, A., Molin, G. & Salviulo, G. Archeological glass alteration products in marine and land-based environments: morphological, chemical and microtextural characterization. *J. Non-Cryst. Solids* **351**, 1338–1349 (2005).
23. Geisler, T. et al. Aqueous corrosion of borosilicate glass under acidic conditions: a new corrosion mechanism. *J. Non-Cryst. Solids* **356**, 1458–1465 (2010).
24. Schalm, O., Nuyts, G. & Janssens, K. Some critical observations about the degradation of glass: the formation of lamellae explained. *J. Non-Cryst. Solids* **569**, <https://doi.org/10.1016/j.jnoncrysol.2021.120984> (2021).
25. Wang, Y., Jove-Colon, C. F., Lenting, C., Icenhower, J. & Kuhlman, K. L. Morphological instability of aqueous dissolution of silicate glasses and minerals. *npj Mater. Degrad.* **2**, 27 (2018).
26. Fryar, D., Nell, R. & Oostrom, M. *Hanford Site Composite Analysis: Radionuclide Selection for Groundwater Pathway Evaluation* (Hanford Site (HNF), 2022).
27. DOE, U. *Performance Assessment for the Integrated Disposal Facility, Hanford Site*. (Washington River Protection Solutions, LLC, 2018).
28. Karl, T. R., Melillo, J. M. & Peterson, T. C. (eds) *Global Climate Change Impacts in the United States: A State of Knowledge Report from the U.S. Global Change Research Program* (Cambridge University Press, 2009).

29. Mote, P. W., Salathé, E. P., Dulière, V. & Jump, E. Scenarios of Future Climate Change for the Pacific Northwest. Report prepared by the Climate Impacts Group, Center for Science in the Earth System, Joint Institute for the Study of the Atmosphere and Oceans, University of Washington, Seattle. <https://doi.org/10.7915/CIG5S757F> (2008).
30. Wing, N., Peterson, K., Whitlock, C. & Burk, R. *Long-term Climate Change Effects Task for the Hanford Site Permanent Isolation Barrier Development Program: Final Report*. BHI-00144 (Bechtel, Hanford, 1995).
31. DOE, U. *Radioactive Waste Management Manual*, US Department of Energy Office of Environmental Management report 435.1-1. (1999).
32. Sjöblom, R. et al. Assessment of the reason for the vitrification of a wall at a hillfort. The example of Broborg in Sweden. *J. Archaeol. Sci. Rep.* **43**, 103459 (2022).
33. Plymale, A. E. et al. Niche partitioning of microbial communities at an ancient vitrified hillfort: implications for vitrified radioactive waste disposal. *Geomicrobiol. J.* **38**, 1–21 (2020).
34. Englund, M., Heimdahl, J., Larsson, F., Magnell, O. & Ogenhall, E. *Broborg Hillfort: A Research Study of the Vitrified Wall. The Archaeologists*. Report No. 2018:103 (National Historical Museums, 2018).
35. Ogenhall, E. *Amphibolitic Rocks Near Broborg, Uppland. Chemical and Mineralogical Analyses of Metamorphic Mafic-intermediate Rocks from Outcrops Near the Prehistoric Vitrified Hillfort Broborg and a Boulder in the Hillfort*. Report No. RAÄ 156:1 (Arkeologerna, 2016).
36. Kresten, P. & Ambrosiani, B. Swedish vitrified forts: a reconnaissance study. *Fornvännen J. Swed. Antiquarian Res.* **87**, 1–17 (1992).
37. McCloy, J. S. et al. Reproduction of melting behavior for vitrified hillforts based on amphibolite, granite, and basalt lithologies. *Sci. Rep.* **11**, 1272 (2021).
38. Sjöström, J. K. et al. Late Holocene peat paleodust deposition in south-western Sweden—exploring geochemical properties, local mineral sources and regional aeolian activity. *Chem. Geol.* **602**, 120881 (2022).
39. Swedish University of Agricultural Sciences (SLU). Digital soil map of Sweden. <https://gis-slu.maps.arcgis.com/apps/StorytellingSwipe/index.html?appid=e55d28b98d2241e0a6c91ae42073b52f> (2017).
40. Ljungqvist, F. C. A new reconstruction of temperature variability in the extra-tropical Northern Hemisphere during the last two millennia. *Geogr. Ann. Ser. A Phys. Geogr.* **92**, 339–351 (2010).
41. Gibbons, A. Why 536 was ‘the worst year to be alive’. <https://www.science.org/content/article/why-536-was-worst-year-be-alive> (2018).
42. Amundsen, B. & Baxilchuk, N. The long harsh Fimbul Winter is not a myth. *Science Norway* 24 (2019).
43. Moberg, A., Sonechkin, D. M., Holmgren, K., Datsenko, N. M. & Karlén, W. Highly variable Northern Hemisphere temperatures reconstructed from low-and high-resolution proxy data. *Nature* **433**, 613–617 (2005).
44. Ilani, S., Flexer, A. & Kronfeld, J. Copper mineralization in sedimentary cover associated with tectonic elements and volcanism in Israel. *Miner. Depos.* **22**, <https://doi.org/10.1007/bf00204519> (1987).
45. Ben-Yosef, E. Back to Solomon’s era: results of the first excavations at ‘Slaves’ Hill’(site 34, Timna, Israel). *Bull. Am. Sch. Orient. Res.* **376**, 169–198 (2016).
46. Western, S. The classification of arid zone soils. *J. Soil Sci.* **23**, 279–297 (1972).
47. Dan, J., Yaalon, D., Moshe, R. & Nissim, S. Evolution of Reg soils in southern Israel and Sinai. *Geoderma* **28**, 173–202 (1982).
48. Ravikovitch, S. *Soil Map of Southern Israel* (Hebrew University of Jerusalem Soil and Water Sciences, 1924).
49. Dan, Y., Raz, Z., Yaalon, H. & Koyumdjisky, H. *Soil Map of Israël* (Survey of Israel, 1975).
50. IUSS Working Group WRB. World Reference Base for Soil Resources 2014, Update 2015. International Soil Classification System for Naming Soils and Creating Legends for Soil Maps. World Soil Resources Reports No. 106, Rome: FAO (2015).
51. Cavanagh, M., Ben-Yosef, E. & Langgut, D. Fuel exploitation and environmental degradation at the Iron Age copper industry of the Timna Valley, southern Israel. *Sci. Rep.* **12**, 15434 (2022).
52. Rosen, S. A. Basic instabilities? Climate and culture in the Negev over the long term. *Geomorphology* **32**, 6–22 (2017).
53. Bar-Matthews, M. & Ayalon, A. Yamin Plain: Present-Day and Paleo Climate Conditions. Geological Survey of Israel Report (2024).
54. Bruins, H. J. Ancient desert agriculture in the Negev and climate-zone boundary changes during average, wet and drought years: ancient agriculture in the Middle East. *J. Arid Environ.* **86**, 28–42 (2012).
55. Alpert, P., Krichak, S. O., Shafir, H., Haim, D. & Osetinsky, I. Climatic trends to extremes employing regional modeling and statistical interpretation over the E. Mediterranean. *Glob. Planet. Change* **63**, 163–170 (2008).
56. Linneman, S. R. & Myers, J. D. Magmatic inclusions in the Holocene rhyolites of Newberry Volcano, central Oregon. *J. Geophys. Res. Solid Earth* **95**, 17677–17691 (1990).
57. MacLeod, N. S. & Sammel, E. Newberry Volcano, Oregon: a cascade range geothermal prospect. *Oregon Geol.* **44**, 123–131 (1982).
58. Hildreth, W. Quaternary magmatism in the Cascades—Geologic perspectives. Reston, Va.: U.S. Geological Survey, 1–125 (2007).
59. Jensen, R. A., Donnelly-Nolan, J. M. & Mckay, D. A field guide to Newberry Volcano, Oregon. In J. E. O’Connor, R. J. Dorsey, & I. P. Madin (Eds.), *Volcanoes to Vineyards: Geologic Field Trips through the Dynamic Landscape of the Pacific Northwest* (Vol. 15, pp. 0). Geological Society of America. [https://doi.org/10.1130/2009.fld015\(03\)](https://doi.org/10.1130/2009.fld015(03)) (2009).
60. USDA. Soil Survey Staff, Natural Resources Conservation Service, United States Department of Agriculture. Web Soil Survey. Available online. <https://www.nrcs.usda.gov/resources/data-and-reports/web-soil-survey> Accessed (2024).
61. Mann, M. E. et al. Global signatures and dynamical origins of the Little Ice Age and Medieval Climate Anomaly. *Science* **326**, 1256–1260 (2009).
62. Gedalof, Z. E., Mantua, N. J. & Peterson, D. L. A multi-century perspective of variability in the Pacific Decadal Oscillation: new insights from tree rings and coral. *Geophys. Res. Lett.* **29**, 57–1–57–4 (2002).
63. Mote, P. W., Hamlet, A. F., Clark, M. P. & Lettenmaier, D. P. Declining mountain snowpack in western North America. *Bull. Am. Meteorol. Soc.* **86**, 39–49 (2005).
64. Golovchak, R. et al. Remedial insight on ageing of glass through the study of ancient man-made artefacts. *Archaeometry* **63**, 312–326 (2021).
65. Angelini, I., Gratuze, B. & Artioli, G. in *The Contribution of Mineralogy to Cultural Heritage* (eds Artioli, G. & Oberti, R.) 87–150 (Mineralogical Society, 2019).
66. Furmanek, W. Antropoinfosfera współczesnego człowieka. *Dydaktyka Inform.* **8**, 49–73 (2013).
67. Furmanek, M. et al. Dobkowice revisited. Interdisciplinary research on an enclosure of the Jordanów culture. *Anthropologie. Int. J. Hum. Diversity Evol.* **51**, 375–396 (2014).
68. Kuznicki, F. Soil Map of Poland [1:2,000,000]. https://esdac.jrc.europa.eu/images/Eudasm/PL/pol_x6.jpg (1984).
69. Lamb, H. Climatic changes in our own times and future threats. *Geography* **67**, 203–220 (1982).
70. Perşoiu, A. et al. Holocene winter climate variability in Central and Eastern Europe. *Sci. Rep.* **7**, 1–8 (2017).
71. Brázdil, R., Pfister, C., Wanner, H., Storch, H. V. & Luterbacher, J. Historical climatology in Europe—the state of the art. *Clim. change* **70**, 363–430 (2005).

72. Przybylak, R. Recent air-temperature changes in the Arctic. *Ann. Glaciol.* **46**, 316–324 (2007).
73. Domonkos, P., Kysely, J., Piotrowicz, K., Petrovic, P. & Likso, T. Variability of extreme temperature events in south-central Europe during the 20th century and its relationship with large-scale circulation. *Int. J. Climatol. A J. R. Meteorol. Soc.* **23**, 987–1010 (2003).
74. Hand, R. J. The Ballidon glass burial experiment—35 years on. *Glass Technol.* **46**, 237–242 (2005).
75. McLoughlin, S. et al. The long term corrosion of glasses: analytical results after 32 years of burial at Ballidon. *Glass Technol. Eur. J. Glass Sci. Technol. Part A* **47**, 59–67 (2006).
76. Thorpe, C. L. et al. Insights into long term glass corrosion mechanisms from the Ballidon experiment. *Npj Mater. Degrad.* **9**, 27 (2025).
77. Nambodri Jr, C. & Wicks, G. *SRL In-situ Tests in the United Kingdom: Part 2, Surface Analyses of SRS Waste Glass Buried for One and Two Years in Limestone at Ballidon, UK*. Report No. WSRC-TP-91-288 (Savannah River Site, 1991).
78. United Kingdom Soil Observatory (UKSO). Soil Map of Derbyshire. <https://mapapps2.bgs.ac.uk/ukso/home.html> (2024).
79. Hallett, S. H., Sakrabani, R., Keay, C. A. & Hannam, J. A. Developments in land information systems: examples demonstrating land resource management capabilities and options. *Soil Use Manag.* **33**, 514–529 (2017).
80. Grahame, M. Charting the UK's changing climate, UK Meteorological Office News. https://metoffice.gov.uk/about_us/press-office/news/weather-and-climate/2021/9120-new-climate-normal (2021).
81. United Kingdom Meteorological Office. UK Climate Averages for Nottingham. <https://www.metoffice.gov.uk/research/climate/maps-and-data-averages> (2024).
82. Jantzen, C. M., Kaplan, D. I., Bibler, N. E., Peeler, D. K. & Plodinec, M. J. Performance of a buried radioactive high level waste (HLW) glass after 24 years. *J. Nucl. Mater.* **378**, 244–256 (2008).
83. Wicks, G. G. US field testing programs and results. *J. Nucl. Mater.* **298**, 78–85 (2001).
84. Weart, W. D. *Evaluation of Salt Beds in New Mexico as a Geologic Repository for Nuclear Waste. [Waste Isolation Pilot Plant (WIPP)]*. Report No. SAND-78-2086C (Sandia Laboratory, 1978).
85. Bacon, D. et al. *Field-Scale Lysimeter Studies of Low-Activity Waste Form Degradation*. Report No. PNNL-27394 (Pacific Northwest National Laboratory, 2018).
86. Neeway, J. J., Emerson, H. P., Asmussen, R. M., Fujii Yamagata, A. L. & Meyer, P. D. Review of intermediate-scale field tests in support of disposal of waste forms. *Chemosphere* **347**, 140625 (2024).
87. Ben-Yosef, E. & Rothenberg, B. *Mining for Ancient Copper: Essays in Memory of Beno Rothenberg* (Eisenbrauns, 2018).
88. Hauptmann, A. *Archaeometallurgy-Materials Science Aspects* (Springer, 2020).
89. Sarel, S. et al. Linda Scott Cummings. ANCIENT COPPER MINES AT NAHAL 'AMRAM, SOUTHERN ARABAH. In *MINING FOR ANCIENT COPPER Essays in Memory of Beno Rothenberg* (ed. Ben-Yosef, E.), 147–177 (TEL AVIV UNIVERSITY SONIA AND MARCO NADLER INSTITUTE OF ARCHAEOLOGY MONOGRAPH SERIES NUMBER 37, 2018).
90. Rothenberg, B. Ancient copper industries in the western Arabah: an archaeological survey of the Arabah, Part 1. *Palest. Explor. Q.* **94**, 5–71 (1962).
91. Rothenberg, B. Archaeo-metallurgical researches in the southern Arabah 1959–1990. Part I: late pottery neolithic to early bronze IV. *Palest. Explor. Q.* **131**, 68–89 (1999).
92. Fletcher, W. The chemical durability of glass. A burial experiment at Ballidon in Derbyshire. *J. Glass Stud.* **14**, 149–151 (1972).
93. Barbana, F., Bertonecello, R., Milanese, L. & Sada, C. Alteration and corrosion phenomena in Roman submerged glass fragments. *J. Non-Cryst. Solids* **337**, 136–141 (2004).
94. Longinelli, A., Silvestri, A., Molin, G. & Salviulo, G. 1.8 ka old glass from the Roman ship *Julia Felix*: glass-water oxygen isotope exchange. *Chem. Geol.* **211**, 335–342 (2004).
95. Hellmann, R. In *Encyclopedia of Glass Science, Technology, History, and Culture*, Vol II (ed. Richet, P.) 831–842 (The American Ceramic Society, 2021).
96. Matthews, B. E. et al. Micro- and nanoscale surface analysis of late iron age glass from Broborg, a vitrified Swedish Hillfort. *Microsc. Microanal.* **29**, 50–68 (2023).
97. Kresten, P., Kero, L. & Chyessler, J. Geology of the vitrified hill-fort Broborg in Uppland, Sweden. *Geologiska Föreningen i Stockholm Förhandlingar* **115**, 13–24 (1993).
98. Vicenzi, E. P. et al. Major to trace element imaging and analysis of iron age glasses using stage scanning in the analytical dual beam microscope (tandem). *Herit. Sci.* **10**, 90 (2022).
99. Samuel, E. A. & Craig, R. W. *Hydrology of the Newberry Volcano Caldera, Oregon*. Report No. 83-4091 (U. S. Geological Survey Report, 1983).
100. Marcial, J. et al. Effect of network connectivity on behavior of synthetic Broborg hillfort glasses. *J. Am. Ceram. Soc.* **106**, 1716–1731 (2023).
101. US DOE. *Performance Assessment for the Integrated Disposal Facility, Hanford Site*. Report No. RPP-RPT-59958, Rev. 1 (Washington River Protection Solutions, LLC, 2018).
102. Weaver, J., MccLoy, J., Ryan, J. V. & Kruger, A. A. Ensuring longevity: ancient glasses help predict durability of vitrified nuclear waste. *Am. Ceram. Soc. Bull.* **95**, 18–23 (2016).
103. Bagwell, C. E. in *Microbial Biotechnology: Energy and Environment* (ed. Arora, R.) 363–381 (Savannah River National Laboratory, 2011).
104. Weaver, J. L. et al. Microbial interactions with silicate glasses. *npj Mater. Degrad.* **5**, 11 (2021).
105. Foster, L. et al. Microbial bloom formation in a high pH spent nuclear fuel pond. *Sci. Total Environ.* **720**, 137515 (2020).
106. Fredrickson, J. K. et al. Geomicrobiology of high-level nuclear waste-contaminated vadose sediments at the Hanford Site, Washington state. *Appl. Environ. Microbiol.* **70**, 4230–4241 (2004).
107. U.S. DOE. *Hanford Site Groundwater Monitoring Report for 2017*. Report No. DOE/RL-2017-66, Rev. 0 (US Department of Energy, Richland Operations Office, 2018).
108. Kim, J.-S., Kwon, S.-K., Sanchez, M. & Cho, G.-C. Geological storage of high level nuclear waste. *KSCE J. Civ. Eng.* **15**, 721–737 (2011).
109. Pierce, E. M. et al. *Waste Form Release Data Package for the 2005 Integrated Disposal Facility Performance Assessment*. Report No. PNNL-14805 (Pacific Northwest National Laboratory, 2004).
110. Thorpe, C. L. et al. Microbial interactions with phosphorus containing glasses representative of vitrified radioactive waste. *J. Hazard. Mater.* **462**, 132667 (2024).
111. Geisler, T. et al. The mechanism of borosilicate glass corrosion revisited. *Geochim. Cosmochim. Acta* **158**, 112–129 (2015).
112. Hellmann, R. in *Encyclopedia of Glass Science, Technology, History, and Culture*, Vol I (ed. Richet, P.) 647–662 (The American Ceramic Society, 2021).
113. Hellmann, R. et al. Nanometre-scale evidence for interfacial dissolution-precipitation control of silicate glass corrosion. *Nat. Mater.* **14**, 307–311 (2015).
114. Paudel, B. et al. ToF-SIMS in material research: a view from nanoscale hydrogen detection. *Mater. Today* **75**, 149–165 (2024).
115. EPA–U.S Environmental Protection Agency. *SW-846 Test Method 3052: Microwave Assisted Acid Digestion of Siliceous and Organically Based Matrices* (U.S. Environmental Protection Agency, 1996).
116. Colman, S. M., Platt Bradbury, J. & Rosenbaum, J. G. Paleolimnology and paleoclimate studies in Upper Klamath Lake, Oregon. *J. Paleolimnol.* **31**, 129–138 (2004).
117. Steinman, B. A., Abbott, M. B., Mann, M. E., Stansell, N. D. & Finney, B. P. 1,500 year quantitative reconstruction of winter precipitation in the Pacific Northwest. *Proc. Natl. Acad. Sci. USA* **109**, 11619–11623 (2012).

118. Büntgen, U. et al. 2500 years of European climate variability and human susceptibility. *Science* **331**, 578–582 (2011).

Acknowledgements

This work is supported by the Waste Treatment and Immobilization Plant Project at the United States Department of Energy (US DOE) Hanford Field Office (HFO). The authors gratefully acknowledge Professor Peter Kresten for supplying the original vitrified samples from Broborg, Professor Sylwester Czopek for help with archeologic data of the Dobkowice sample, and Nathan Canfield for performing X-ray CT of one sample. A portion of the research was performed using the Environmental Molecular Sciences Laboratory (EMSL), a national scientific user facility sponsored by the DOE's Office of Biological and Environmental Research located at Pacific Northwest National Laboratory under proposal number 60748 (Award <https://doi.org/10.46936/lr.proj.2023.60748/60008973>). Pacific Northwest National Laboratory is operated for the DOE by Battelle Memorial Institute under Contract DE-AC06-76RLO 1830.

Author contributions

J. Marcial, J. Chesnutt, J.N., C.P., R.G., R. Hand, C.T., E.B., J. McCloy, D.K., R. Hellmann, R.S. and A. Kruger wrote the main manuscript text. Z.Z. performed ToF-SIMS measurements. A.D. and S.L. performed XCT measurements. L.B., E.G., O.Y., E.B. and D.K. provided Timna samples and wrote sections related to Timna. R.H. and C.T. provided data for Ballidon and wrote Ballidon section. R.G., J. Cebulski, P.N. and M. Szostek provided Dobkowice samples. M. Schweiger provided Newberry samples and project guidance. S.C., J.H., A.P., N.B., R.A. and A. Kennedy performed laboratory measurements. All authors reviewed the manuscript. Retired: Michael J. Schweiger.

Competing interests

The authors declare no competing interests.

Additional information

Supplementary information The online version contains supplementary material available at <https://doi.org/10.1038/s41529-025-00624-4>.

Correspondence and requests for materials should be addressed to Jose Marcial.

Reprints and permissions information is available at <http://www.nature.com/reprints>

Publisher's note Springer Nature remains neutral with regard to jurisdictional claims in published maps and institutional affiliations.

Open Access This article is licensed under a Creative Commons Attribution-NonCommercial-NoDerivatives 4.0 International License, which permits any non-commercial use, sharing, distribution and reproduction in any medium or format, as long as you give appropriate credit to the original author(s) and the source, provide a link to the Creative Commons licence, and indicate if you modified the licensed material. You do not have permission under this licence to share adapted material derived from this article or parts of it. The images or other third party material in this article are included in the article's Creative Commons licence, unless indicated otherwise in a credit line to the material. If material is not included in the article's Creative Commons licence and your intended use is not permitted by statutory regulation or exceeds the permitted use, you will need to obtain permission directly from the copyright holder. To view a copy of this licence, visit <http://creativecommons.org/licenses/by-nc-nd/4.0/>.

© The Author(s) 2025